

AperTO - Archivio Istituzionale Open Access dell'Università di Torino

**Heat capacity of hydrous trachybasalt from Mt Etna: comparison with  $\text{CaAl}_2\text{Si}_2\text{O}_8$  (An)- $\text{CaMgSi}_2\text{O}_6$  (Di) as basaltic proxy compositions**

**This is a pre print version of the following article:**

*Original Citation:*

*Availability:*

This version is available <http://hdl.handle.net/2318/1544274> since 2017-05-12T17:32:55Z

*Published version:*

DOI:10.1007/s00410-015-1196-6

*Terms of use:*

Open Access

Anyone can freely access the full text of works made available as "Open Access". Works made available under a Creative Commons license can be used according to the terms and conditions of said license. Use of all other works requires consent of the right holder (author or publisher) if not exempted from copyright protection by the applicable law.

(Article begins on next page)

# Contributions to Mineralogy and Petrology

## Heat capacity of hydrous trachybasalt from Mt Etna: comparison with $\text{CaAl}_2\text{Si}_2\text{O}_8$ (An) - $\text{CaMgSi}_2\text{O}_6$ (Di) as basaltic proxy compositions --Manuscript Draft--

<b>Manuscript Number:</b>	CTMP-D-15-00019R1
<b>Full Title:</b>	Heat capacity of hydrous trachybasalt from Mt Etna: comparison with $\text{CaAl}_2\text{Si}_2\text{O}_8$ (An) - $\text{CaMgSi}_2\text{O}_6$ (Di) as basaltic proxy compositions
<b>Article Type:</b>	Original Paper
<b>Keywords:</b>	specific heat, viscosity, thermochemical and transport properties, hydrous Etna trachybasalt, anorthite-diopside-water system
<b>Corresponding Author:</b>	Daniele Giordano, Faculty (Research position) Universita degli Studi di Torino Torino, ITALY
<b>Corresponding Author Secondary Information:</b>	
<b>Corresponding Author's Institution:</b>	Universita degli Studi di Torino
<b>Corresponding Author's Secondary Institution:</b>	
<b>First Author:</b>	Daniele Giordano, Faculty (Research position)
<b>First Author Secondary Information:</b>	
<b>Order of Authors:</b>	Daniele Giordano, Faculty (Research position) Alex Rober Nichols, PhD Marcel Potuzak, PhD Danilo Di Genova, PhD Claudia Romano, Faculty (associate professor) James Kelly Russell, Faculty (full professor)
<b>Order of Authors Secondary Information:</b>	
<b>Funding Information:</b>	
<b>Abstract:</b>	<p>The specific heat capacity (<math>C_p</math>) of six variably-hydrated (~ 3.5 wt% <math>\text{H}_2\text{O}</math>) iron-bearing Etna trachybasaltic glasses and liquids has been measured using differential scanning calorimetry from room temperature across the glass transition region. These data are compared to heat capacity measurements on thirteen melt compositions in the iron-free anorthite (An) - diopside (Di) system over a similar range of <math>\text{H}_2\text{O}</math> contents. These data extend considerably the published <math>C_p</math> measurements for hydrous melts and glasses. The results for the Etna trachybasalts show non-linear variations in, both, the heat capacity of the glass at the onset of the glass transition (i.e. <math>C_{pg}</math>) and the fully relaxed liquid (i.e. <math>C_{pl}</math>) with increasing <math>\text{H}_2\text{O}</math> content. Similarly, the "configurational heat capacity" (i.e. <math>C_{pc} = C_{pl} - C_{pg}</math>) varies non-linearly with <math>\text{H}_2\text{O}</math> content. The An-Di hydrous compositions investigated show similar trends, with <math>C_p</math> values varying as a function of melt composition and <math>\text{H}_2\text{O}</math> content. The results show that values in hydrous <math>C_{pg}</math>, <math>C_{pl}</math> and <math>C_{pc}</math> in the depolymerized glasses and liquids are substantially different from those observed for more polymerized hydrous albitic, leucogranitic, trachytic and phonolitic multicomponent compositions previously investigated by Bouhifd et al. (2006). Polymerized melts have lower <math>C_{pl}</math>, <math>C_{pc}</math> and higher <math>C_{pg}</math> with respect to more depolymerized compositions. The covariation between <math>C_p</math> values and the degree of polymerization in glasses and melts is well described in terms of a modified SMhydrous, and NBO/Thydrous. Values of <math>C_{pc}</math> increase sharply with increasing depolymerization up to SMhydrous ~30-35 mol % (NBO/Thydrous ~ 0.5) then decrease to an almost constant value.</p> <p>The partial molar heat capacity of <math>\text{H}_2\text{O}</math> for both glasses (<math>C_{pg}\text{H}_2\text{O}</math>) and liquids</p>

	<p>(CpIH<sub>2</sub>O) appears to be independent of composition and, assuming ideal mixing, we obtain a value for CpIH<sub>2</sub>O of 79 J mol<sup>-1</sup> K<sup>-1</sup>. However, we note that a range of values for CpIH<sub>2</sub>O (i.e. ~ 78 - 87 J mol<sup>-1</sup> K<sup>-1</sup>) proposed by previous workers will reproduce the extended data to within experimental uncertainty. Our analysis suggests that more data are required in order to ascribe a compositional dependence (i.e. non-ideal mixing) to CpIH<sub>2</sub>O.</p>
<p><b>Response to Reviewers:</b></p>	<p>Reply to comments/suggestions/additions  REVIEWER 1</p> <p>1. Sample description.  The reviewer is interested in knowing more about the effect of iron species on structure and how this would affect the calculation of SM parameters. Here is a more detailed explanation of the reasons why we considered treating half of the total iron as a network former and other half as a network modifier in order to calculate the SM parameters.</p> <p>Iron speciation of hydrous samples was not measured in this paper and the assumed role of iron and water species is described in paragraph 3.2 (line 221 - 233 of the original manuscript). Di Muro et al. (2009) showed that basalts demonstrate that the sensitivity of glass structure to changing redox conditions decreases with increasing depolymerization. Mercier et al. (2009, 2010), based on a large number of measurements on various compositions, showed that water (i.e. hydrous melts) has a depolymerizing effect that seems to be independent from that of the other modifying components. Similarly it has been demonstrated by Giordano et al. (2008b) that the role of water on the structure is somehow independent from that of the other cations. However, in rare cases, such as for basaltic compositions it could also slightly increase the polymerization of the structure (Giordano et al., 2009b GCA).</p> <p>In order to know the exact role of the effective network modifiers and the role of iron species in the network structure further extensive research is required. This is not the objective and beyond the scope of this study. In particular, for hydrous melts this work would require much more than the just accurate measurements of iron partitioning. Even in anhydrous melts the effective partitioning of Fe and the structural role of Fe species is still poorly known (both Fe<sup>2+</sup> and Fe<sup>3+</sup> can have network former (coordination IV) and network modifier (coordination VI) or intermediate (coordination V) roles depending on the compositions). The role of iron in hydrous melts is even more complicated and has only been discussed in a few papers (e.g., Mercier et al., 2009; 2010 and Di Muro et al., 2009). Mercier et al., (2009; 2010) and Di Muro et al. (2009) use the same basaltic composition as that used here and are based on large sample statistics. They show that our decision of assuming iron as partitioned half as a FeO and half as Fe<sub>2</sub>O<sub>3</sub> is the best choice we can make so far. Based on the data currently available, the SM<sub>hydrous</sub> parameter is the best estimation that can be made at present. Di Muro et al. (2009) is now referred to in the manuscript where readers can find the evaluation and the significance of the uncertainty of the calculated SM/SM<sub>hydrous</sub> parameters.</p> <p>On the basis of what is mentioned above, I believe that the role of iron species on anhydrous and hydrous basaltic glasses would have no significant effect in the structure nor in the calculation of the SM parameter.</p> <p>2. We have added a small paragraph and two figures (as supporting online material) to describe the procedure used to perform the sensitivity calibration and calculate measurement accuracy.</p> <p>3. The selected cooling/heating rate that we used for the calculation is, as reported at line 157 of the original manuscript, 10 K/min.</p> <p>4. We changed it and, in order to be clearer about the role of pressure on the samples synthesized at high pressure, we have re-phrased that part of the paragraph, from line 149 to 158 of the new manuscript version.</p> <p>5. These are the ways of expressing the same meaning, but we are happy to use the terms suggested by the reviewer. It has been modified throughout.</p> <p>6. Corrected.</p> <p>7. Corrected, we have changed it to match the journal style that requires J mol<sup>-1</sup> K<sup>-1</sup> to</p>

be used.

8. Done

9. Done

10. The way how both NBO/T and SM parameters are calculated is explained on lines 221-233 of the original manuscript, as following:

Lines 224 to 226 state: " The modified SM parameter, referred to hereafter as SMhydrous, is calculated, in mol%, as the sum of the network modifier oxides plus the amount of dissolved H<sub>2</sub>O (Giordano et al. 2009; Mercier et al. 2009), without accounting for H<sub>2</sub>O speciation."

Lines 227 to 232 state: "Both the SMhydrous and NBO/Thydrous are considered to be representative of the degree of polymerization of the hydrous liquids (Mysen, 1988; Giordano et al. 2009) and both of them were calculated assuming, according to Mercier et al. (2009) and Di Muro et al. (2009) that half of the FeO<sub>tot</sub> (in wt%) partitions as FeO and the other half as Fe<sub>2</sub>O<sub>3</sub>, that implies a nearly constant [Fe<sub>2</sub>O<sub>3</sub>/(FeO + Fe<sub>2</sub>O<sub>3</sub>)] mass ratio value of about 0.5."

11. As explained above in reply to point one and discussed by Di Muro et al. (2009) - also referred to in the original manuscript iron speciation is not expected to significantly effect the structure of melts. As a consequence the effect of pressure will be not important. In addition, all samples are thermally re-equilibrated at atmospheric conditions during the first heating state and the pressure and thermal history undergone during hydrothermal syntheses will have even less of an effect.

12. Done.

13. Done.

14. We have added a legend to the figure.

15. Corrected.

16. The answer to this point is given in the response to point 11. We have added the following sentence to the manuscript to make it clearer: "Nonetheless, the heating cycles that each sample has gone will remove the thermal history that the sample experienced during its synthesis, resulting in sample equilibration at conditions similar to atmospheric under argon flow to prevent oxidation."

17. The values of T<sub>gonset</sub> and T<sub>liquid</sub> are used in the manuscript were calculated in the most accurate way from the heat capacity data according to the configurational entropy theory.

Other papers show the effect of heating/cooling rates on the glass transition temperatures and the specific viscosity values associated with it (e.g. Giordano et al., 2005, 2008b). Taking T<sub>g</sub> as the temperature where viscosity is 10<sup>12</sup> Pa s is just a comfortable approximation used in industrial science to compare it at the timescale of forming processes (about 100-1000 s) and is used here for convenience as it can be calculated from viscosity measurements. Industry actually defines 10<sup>12.2</sup> Pa s viscosity value as the "annealing point". There are two standard ASTM measurements using fiber elongation and beam bending techniques (ASTM C336 and C1350M).

18. The T<sub>gonset</sub> of a glass which was previously cooled at 10K/min through the glass transition temperature region and subsequently heated up at 10K/min will exhibit T<sub>gonset</sub> equal to the temperature where viscosity is ~10<sup>12</sup> Pa s. This seems to be universal in oxide and silica base glasses.

REVIEWER 2.

Line 148: A column reporting the values of the mass of the samples investigated in this work has been added to Table 1 and the text has been changed accordingly.

Line 154: We have slightly modified the text (lines from 169 to 178) to provide some additional information about the DSC experimental procedure.

Line 157: We have added a small paragraph (lines 179 to 186 in the revised manuscript) to explain how many thermal cycles the samples experienced and how the samples were inspected to check for any potential change/instability due to the thermal treatments.

Line 173: We have added some more details (lines 179- 186) described how we checked sample stability after the DSC experiments.

Line 182: We have added a legend to Fig. 2b.

With regard to error bars, we have added the following sentence on lines 156-158: "Based on multiple heating and cooling scans we believe reproducibility to be better than 3%. Therefore error bars for the  $C_p$  values of the fully relaxed liquid ( $C_{pl}$ ) or  $C_p$  values of the glass ( $C_{pg}$ ) are smaller than the symbol size used in the figures." With regard to the number of measurements, yes, the presented data are based on one measurement at matching cooling and heating rates of 10 K/min for each sample. However, each sample experienced multiple thermal cycles (see lines 175-184 for a more detailed description of the measurement procedure) and inspected the samples before and after the DSC experiments.

Line 200: See previous comment and lines 146 - 158.

Lines 230 to 233 and line : We have modified the text and added a reference to Di Muro et al. (2009) who measured the redox state of various glasses (basalts in particular). Please also see comment to reviewer #1 (point 1).

Line 263: Letters were added to each figure in order to identify panels. Thank you for the suggestion.

Line 275: Legend was added for sake of clarity as suggested by the reviewer. Thank you.

Line 282-287 (now 312): The word "minima" was referred to trends observed in Fig. 4B. We have slightly modified the text in order to clarify it.

Lines 323-325 (now line 354-357 and added new text from line 358 - 378): here we have explained (having significantly extended the database of comparison for the heat capacity of hydrous melts compared to the previous work by Bouhifd et al. 2006, 2013) on which statistical parameters (standard deviation and average relative error) we decided to choose a best fit value of  $79 \text{ J mol}^{-1} \text{ K}^{-1}$  for the partial molar heat capacity of water. We also explain that the difference between our value and the value of  $85 \text{ J mol}^{-1} \text{ K}^{-1}$  proposed by Bouhifd et al. (2006) is rather insignificant. However, the value of  $257 \text{ J mol}^{-1} \text{ K}^{-1}$ , proposed by Bouhifd et al. 2013 does not reproduce the data as well using all models.

Lines 326 - 343: We have inserted a new paragraph describing the glass transition variation.

Line 464: we replaced steeply with steadily.

1                   **Heat capacity of *hydrous* trachybasalt from Mt Etna: comparison with**  
2                   **CaAl<sub>2</sub>Si<sub>2</sub>O<sub>8</sub> (An) – CaMgSi<sub>2</sub>O<sub>6</sub> (Di) as basaltic proxy compositions**

3  
4  
5                   D. Giordano<sup>a</sup>, A.R.L. Nichols<sup>b</sup>, M. Potuzak<sup>c</sup>, D. Di Genova<sup>d</sup>, C. Romano<sup>e</sup> and J.K.  
6                   Russell<sup>f</sup>

7  
8                   <sup>a</sup>Dipartimento di Scienze della Terra, Universita' degli Studi di Torino, Via Valperga Caluso 35,  
9                   10125 Torino, Italia

10  
11                   <sup>b</sup>Research and Development Center for Ocean Drilling Science, Japan Agency for Marine Earth  
12                   Science and Technology (JAMSTEC), 2-15 Natsushima-cho, Yokosuka, Kanagawa, 237-0061,  
13                   Japan

14  
15                   <sup>c</sup>Science and Technology Division, Corning Incorporated, Corning, 14831 NY, USA

16  
17                   <sup>d</sup>Department for Earth and Environmental Sciences, University of Munich, Theresienstraße 41/III,  
18                   80333 Munich, Germany

19  
20                   <sup>e</sup>Dipartimento di Scienze, Università degli Studi Roma Tre, L.go San Leonardo Murialdo 1, 00146  
21                   Rome, Italia

22  
23                   <sup>f</sup>Department of Earth, Ocean and Atmospheric Sciences, The University of British Columbia,  
24                   Vancouver, British Columbia, V6T 1Z4

25  
26  
27  
28                   Corresponding author details

29  
30                   phone: +39 011 670 5110

31                   fax: +39 011 670 5128

32                   e-mail: [daniele.giordano@unito.it](mailto:daniele.giordano@unito.it)

33  
34                   **Keywords:** specific heat, Etna trachybasalt, anorthite-diopside, hydrous silicate melts

35  
36                   Submitted to

37                   Contributions to Mineralogy and Petrology

38                   January 20, 2015

39                   Revised September 24, 2015

## Abstract

The specific heat capacity ( $C_p$ ) of six variably-hydrated ( $\sim 3.5$  wt%  $H_2O$ ) iron-bearing Etna trachybasaltic glasses and liquids has been measured using differential scanning calorimetry from room temperature across the glass transition region. These data are compared to heat capacity measurements on thirteen melt compositions in the iron-free anorthite (An) - diopside (Di) system over a similar range of  $H_2O$  contents. These data extend considerably the published  $C_p$  measurements for hydrous melts and glasses. The results for the Etna trachybasalts show non-linear variations in, both, the heat capacity of the glass at the onset of the glass transition (i.e.  $C_p^g$ ) and the fully relaxed liquid (i.e.  $C_p^l$ ) with increasing  $H_2O$  content. Similarly, the “configurational heat capacity” (i.e.  $C_p^c = C_p^l - C_p^g$ ) varies non-linearly with  $H_2O$  content. The An-Di hydrous compositions investigated show similar trends, with  $C_p$  values varying as a function of melt composition and  $H_2O$  content. The results show that values in hydrous  $C_p^g$ ,  $C_p^l$  and  $C_p^c$  in the depolymerized glasses and liquids are substantially different from those observed for more polymerized hydrous albitic, leucogranitic, trachytic and phonolitic multicomponent compositions previously investigated by Bouhifd et al. (2006). Polymerized melts have lower  $C_p^l$ ,  $C_p^c$  and higher  $C_p^g$  with respect to more depolymerized compositions. The covariation between  $C_p$  values and the degree of polymerization in glasses and melts is well described in terms of a modified  $SM_{hydrous}$ , and  $NBO/T_{hydrous}$ . Values of  $C_p^c$  increase sharply with increasing depolymerization up to  $SM_{hydrous} \sim 30$ -35 mol % ( $NBO/T_{hydrous} \sim 0.5$ ) then decrease to an almost constant value.

The partial molar heat capacity of  $H_2O$  for both glasses ( $C_{p^{H_2O}}^g$ ) and liquids ( $C_{p^{H_2O}}^l$ ) appears to be independent of composition and, assuming ideal mixing, we obtain a value for  $C_{p^{H_2O}}^l$  of 79 J mol<sup>-1</sup> K<sup>-1</sup>. However, we note that a range of values for  $C_{p^{H_2O}}^l$  (i.e.  $\sim 78$  - 87 J mol<sup>-1</sup> K<sup>-1</sup>) proposed by previous workers will reproduce the extended data to within experimental uncertainty. Our analysis suggests that more data are required in order to ascribe a compositional dependence (i.e. non-ideal mixing) to  $C_{p^{H_2O}}^l$ .

## 1. Introduction

The thermophysical properties of silicate melts are of fundamental importance for the characterization of the dynamics and energetics of silicate melts on Earth. Heat capacity is one such property and the isobaric heat capacities of silicate glasses and liquids are important for thermal modelling of magmatic and volcanic processes (i.e., mingling and mixing, partial melting and solidification, advection of heat, degassing) (e.g. Burnham and Davis, 1974; Clemens and Navrotsky 1987; Russell 1990; Sahagian and Proussevich 1996; Perugini and Poli 2005), to the energy budgets of volcanic eruptions (e.g. Pyle 1995), and for constraining phase equilibria models (Sack and Ghiorso 1989; Ghiorso and Sack 1995). Perhaps more importantly, they provide an important linkage between macroscopic thermochemical properties of melts and their corresponding structural and transport properties (e.g. Richet and Bottinga 1995; Giordano et al. 2009; Chevrel et al. 2013).

Several studies have investigated the specific heat capacity ( $C_p$ ) of anhydrous (i.e.  $H_2O < 500$  ppm) melts (e.g., Navrotsky, 1995; Toplis et al. 2001). However, given the inherent difficulties in conducting equivalent experiments on hydrous melts, only a few studies (i.e. Giordano et al. 2005, 2008a; Bouhifd et al. 2006; 2013, Di Genova et al. 2014) have measured the calorimetric properties of hydrous multicomponent melts to date. Previous calorimetric measurements (Clemens and Navrotsky; 1987) and thermodynamic modeling (Burnham and Davis, 1974) of the albite- $H_2O$  system estimated the partial molar heat capacity of dissolved  $H_2O$  in silicate liquids ( $C_p^{l_{H_2O}}$ ) at between 78 and 87  $J mol^{-1} K^{-1}$ .

All previous studies investigated *iron-free* multicomponent hydrous silicates and established that the contribution of  $H_2O$  to the  $C_p$  of silicate glasses is small, temperature dependent, and largely independent of composition. Bouhifd et al. (2006) investigated hydrous, silica-rich, polymerized melt compositions, including phonolite, trachyte, leucogranite and albite, and reported  $C_p^{l_{H_2O}}$  as independent of melt composition and to have a value for 85  $J mol^{-1} K^{-1}$ . In contrast, a more recent paper by Bouhifd et al. (2013) investigating silica-poor, hydrous, depolymerized compositions (i.e.,



93 tephritic and foiditic) reported a value for  $C_p^{l_{H_2O}}$  of  $H_2O$  of  $237 \pm 40 \text{ J mol}^{-1} \text{ K}^{-1}$ . The authors  
1  
24 ascribed this difference in estimated values to a strong compositional dependence of the partial  
3  
4  
5 molar heat capacity of  $H_2O$ . The contradiction between the Bouhifd studies and the previous studies  
6  
76 (Burnham and Davis, 1974; Clemens and Navrotsky, 1987) highlights the need for further  
8  
9  
97 investigations to establish what role  $H_2O$  plays in determining the  $C_p$  of multicomponent hydrous  
10  
11  
128 liquids and glasses and how this can be parameterized and modeled.  
13

14  
15 Here we have investigated the heat capacities of hydrous glasses and liquids of a natural  
16  
1700 trachybasalt from Etna and of liquids along the An-Di join. The viscosities and glass transition  
18  
191 temperatures for these melts were previously measured by Giordano and Dingwell (2003) and  
20  
21 Giordano et al. (2005, 2008), respectively. The compositions investigated here were chosen for  
22  
23  
2403 three main reasons. The composition of the Etna trachybasalt represents one of the most common  
25  
26  
2704 natural volcanic rock compositions on Earth. It is iron-bearing and  $H_2O$ -bearing and has glass-  
28  
295 forming ability easily detectable by differential scanning calorimetry (DSC) (e.g. Giordano et al.  
30  
31  
3206 2005; Potuzak et al. 2009). Secondly, the An-Di- $H_2O$  system is of general interest to geochemists as  
33  
3407 well as to petrologists because it serves as a simple analogue for basaltic compositions (e.g.,  
35  
3608 Bowen, 1915; Kushiro, 1973; Weill et al. 1980; Navrotsky et al. 1980). In this study we test the  
37  
38  
3909 degree to which An-Di liquids are good analogues for basalts by comparing the measured  
40  
4110 calorimetric properties of hydrous trachybasaltic glasses and liquids with those in the An-Di- $H_2O$   
42  
43  
4411 system. Thirdly, the wide range of compositions investigated here allows us to explore other  
45  
462 thermochemical properties of hydrous silicate melts. We finally combined these measurements with  
47  
48  
4913 the corresponding viscosity datasets in order to model the configurational entropies at the glass  
50  
5114 transition and establish the correlation between transport and thermochemical properties according  
52  
5315 to the Adam and Gibbs theory of configurational entropy.  
54  
55

## 58 2. Experimental methods 59

### 60 2.1. Sample description 61

119 The methods used to synthesize the samples and characterize their compositions and H<sub>2</sub>O  
1 contents are well established in the literature (e.g., Giordano and Dingwell, 2003; Giordano et al.  
120 2005; 2008) and, thus, only briefly summarized here. The starting materials for the hydrous melts in  
121 the An-Di system belong to a selection of dry glasses used by Knoche et al. (1993) and have the  
122 following compositions: An<sub>10</sub>Di<sub>90</sub>, An<sub>42</sub>Di<sub>58</sub>, An<sub>90</sub>Di<sub>10</sub> and An<sub>100</sub> (Giordano et al. 2008). The  
123 starting material for the Etna trachybasalt is from Giordano and Dingwell (2003). H<sub>2</sub>O-bearing  
124 samples, containing up to ~ 3.5 wt% H<sub>2</sub>O were synthesized using an internally heated pressure  
125 vessel at the IMH (Institute of Mineralogy, University of Hannover, Germany) and the piston  
126 cylinder apparatus available at the BGI (Bavarian Geoinstitute, University of Bayreuth, Germany).  
127 The run products consisted of crystal-free, translucent glasses with no visible bubbles.  
128

129 After high pressure syntheses, the samples were cut into 0.3 to 1 mm thick disks and doubly  
130 polished in preparation for calorimetry measurements. Compositions are reported in previous works  
131 from Giordano et al. (2005, 2008) and calculated compositional parameters for the investigated  
132 samples are reported in Table 1. Prior to the calorimetry measurements, the distribution,  
133 homogeneity and absolute H<sub>2</sub>O content of the disks were measured using FTIR spectroscopy and  
134 Karl-Fisher Titration (KFT), the latter following the method described by Behrens et al. (1996). The  
135 measured H<sub>2</sub>O contents are reported in Table 1 together with their associated uncertainties  
136 (corrected for 0.17 wt% unextracted H<sub>2</sub>O; cf. Behrens et al. 1996).  
137

## 138 2.2. Calorimetric heat capacity measurements of glasses and liquids

139 Calorimetry measurements were performed using a differential scanning calorimeter  
140 (NETZSCH® DSC 404 Pegasus) at the Department of Earth and Environmental Sciences,  
141 University of Munich, Germany, under high purity argon gas to prevent oxidation of iron. The  
142 thermocouples of the DSC were calibrated using the transformation temperatures of the standard  
143 salts, RbNO<sub>3</sub>, KClO<sub>4</sub>, CsCl and K<sub>2</sub>CrO<sub>4</sub>. The sensitivity of the DSC was calibrated using a single  
144 sapphire crystal standard. A baseline heat flow was established by measuring the calorimetric

145 response of two empty Pt/Rh crucibles in order to be able to calculate  $C_p$ . Then the heat flow of a  
146 single sapphire crystal, placed in one of the crucibles, against the empty crucible was measured. The  
147 DSC was calibrated at standard heating rate of 10K/min with the sapphire disk cut from single  
148 crystal sapphire perpendicular to the crystalline c-axis. Both upper and lower flat surfaces were  
149 polished in order to achieve an excellent contact and heat transfer between the platinum crucible  
150 and the sapphire disk placed flat on the bottom of the crucible. A comparison between the multiple  
151 calibration runs performed by using our calorimeter are reported in Fig A ( supporting material  
152 online) compared with the ASTM E1269-5 reference standard. This figure shows that there was an  
153 excellent agreement between the reference  $C_p$  data and our own measurements performed up to  
154 1261 K (Fig A, supporting online material). The accuracy of the experiments was calculated to be  
155 within +/- 1% (Fig. B, supporting online material).. Based on multiple heating and cooling scans we  
156 believe reproducibility to be better than 3%. Therefore error bars for the  $C_p$  values of the fully  
157 relaxed liquid ( $C_p^l$ ) or  $C_p$  values of the glass ( $C_p^s$ ) are smaller than the symbol size used in the  
158 figures.

159 Finally, the heat flow of a doubly polished glass sample disk (or portion of a disk), placed in  
160 one of the crucibles, was measured against the empty crucible. The masses of the sapphire standards  
161 used in the experiments were 27.77 or 55.90 mg; the mass of the sample analysed was as close to  
162 this as possible. Commonly the masses of the samples were matching the mass of sapphire standard,  
163 used as a calibration material for  $C_p$  , within the  $\pm 15\%$  . In the case of sample 802 only, due to the  
164 scarcity of available material, the mass was half that of the standard. We decided to keep the data  
165 related to this sample because it agrees with the overall pattern exhibited by the other Etna samples  
166 measured here and in Di Genova et al (2014). Heating across the glass transition into the  
167 supercooled liquid region started at 40 °C and was conducted cooling/heating at 1 atm under high  
168 purity argon gas to prevent oxidation of iron (Giordano et al. 2005, 2008). In order to allow  
169 complete structural relaxation, samples were initially heated above the glass transition temperature  
170 into the supercooled liquid field (Fig. 1) where the sample relaxed removing any memory of its

171 thermal and high pressure history obtained during experimental synthesis (Giordano et al. 2008a).  
1  
172 This initial heating was conducted at 20 K/min (for the Etna samples) and 10 K/min (for the An-Di  
3  
173 samples). Then the sample was cooled to 40 °C at 20 K/min before being heated above the glass  
4  
6  
174 transition temperature again at a matching heating rate. This cooling and heating cycle was repeated  
8  
9  
175 three more times at matching cooling and subsequent heating rates of 15, 10, 5 K/min. The time  
10  
11  
176 spent above the glass transition temperature during each thermal cycle was kept at a minimum (on  
13  
14  
177 the order of 100 s) in order to prevent H<sub>2</sub>O exsolution. After the measurements were completed for  
15  
16  
178 each sample, the sample was removed from the DSC at room temperature and thoroughly inspected  
18  
19  
179 via optical microscopy for a) clarity b) formation of defects, such as bubbles, crystalline phases and  
20  
21  
180 microscopic phase separations. Additionally the dissolved water content of the sample that had  
22  
23  
24  
181 undergone the DSC experiments was measured by FTIR and compared with the original sample.  
25  
26  
182 Here we only report data from those samples that did not exhibit any changes after having  
27  
28  
283 undergone the four thermal cycles during the DSC measurements. The  $C_p$  values for the glass and  
30  
31  
184 liquid were determined based on the measurements conducted during heating at 10 K/min after  
32  
33  
345 cooling at the same rate.

366 Figure 1 shows the variation of  $C_p$  as a function of temperature for one of the investigated  
37  
38  
387 samples cooling/heating during heating at 10 K/min after cooling at 10 K/min. The  $C_p$  of the glass  
40  
41  
188 ( $C_p^g$ ) at the temperature of the onset of the glass transition ( $T_g^{onset}$ ) is calculated by fitting a Maier–  
42  
43  
189 Kelley (MK) equation ( $C_p^g = a+bT+c/T^2+d*T^{0.5}$ ; where T is the absolute temperature and a, b, c,  
44  
45  
490 d are adjustable parameters, Maier–Kelley, 1932) to the part of the  $C_p$ -curves preceding the onset of  
47  
48  
191 the glass transition ( $<T_g^{onset}$ ). The parameters used in the MK equation for each of the investigated  
49  
50  
5192 samples are provided in Table 1. The MK curve is extrapolated to  $T_g^{onset}$ , which is defined as the  
52  
53  
533 temperature at which the extrapolated  $C_p^g$  intersects the extrapolated rapid increase in  $C_p$  associated  
54  
55  
534 with the glass transition, as described by Moynihan (1995).  $C_p^l$  is defined as the  $C_p$  of the fully  
57  
58  
195 relaxed liquid at the temperature of the stable liquid ( $T_g^{liquid}$ ) in the heat capacity curve, and the  
59  
60  
196 “configurational heat capacity”,  $C_p^c$ , is defined as the difference between  $C_p^l$  and the  $C_p^g$ .

197 Values of  $T_g^{onset}$  and  $T_g^{liquid}$  for the Etna trachybasalts and for the An-Di samples are reported  
1  
198 in Table 1. Values at  $T_g^{onset}$  (Giordano et al. 2005; Giordano et al. 2008) and  $T_g^{liquid}$  (this study) were  
3  
199 used to calculate  $C_p^g$  and  $C_p^l$  according to the model of Richet (1987) and Richet and Bottinga  
5  
200 (1985), which assumes that the partial molar heat capacities of  $Al_2O_3$  and  $TiO_2$  depend on  
8  
201 temperature.

### 203 3. Results

#### 204 3.1. Effects of $H_2O$ on the $C_p$ of Etna and An-Di glasses and liquids

205 The measured  $C_p^g$ ,  $C_p^l$  and  $C_p^c$  values are reported in Table 1 and their variations as a  
20  
206 function of composition are discussed below.

##### 208 3.1.1. Specific heat capacity of hydrous glasses ( $C_p^g$ )

209 For all compositions investigated, increased  $H_2O$  content causes a small decrease in  $C_p^g$   
30  
210 (Fig. 2) defining a slight curving upwards trend. Fig. 2a shows that the  $C_p^g$  of the Etna trachybasalts  
32  
211 (dashed curve and empty triangles) has only a minor decrease ( $\sim 7\%$ ), from about 75.8 to 70.5  $J\ mol^{-1}$   
35  
212  $\cdot K^{-1}$  for  $H_2O$  content up to 2.31 wt% (6.92 mol%). Further addition of  $H_2O$  up to 3.46 wt% (11.39  
37  
213 mol%) produces a slight increase in  $C_p^g$  to 71.5  $J\ mol^{-1}\ K^{-1}$ . Sample An<sub>10</sub> also exhibits a slight  
40  
214 increase in  $C_p^g$ , from 59.9 to 61.4  $J\ mol^{-1}\ K^{-1}$ , upon addition of  $H_2O$  from 1.75 to 2.58 wt% (5.26 to  
42  
215 7.62 mol%) (Fig. 2b). All other samples along the Di-An join show a small but systematic decrease  
45  
216 in  $C_p^g$  with  $H_2O$ . In general (Fig. 2b), the glasses of the An-Di system show parallel patterns that  
47  
217 mimic that followed by Etna trachybasalt (dashed curves). The absolute values of  $C_p^g$  are very  
50  
218 similar for An<sub>100</sub>, An<sub>90</sub> and Etna (dashed curve) whereas they decrease slightly but systematically  
52  
219 for An<sub>42</sub> and An<sub>10</sub> compositions. For instance, at 5 mol%  $H_2O$ ,  $C_p^g$  of An<sub>100</sub>, An<sub>90</sub>, Etna, An<sub>42</sub>, An<sub>10</sub>  
54  
220 are calculated to be  $\sim 77, 74, 72, 66$  and  $60\ J\ mol^{-1}\ K^{-1}$ , respectively (see Table 1 for  $C_p$  values). The  
55  
221 dissolution of  $H_2O$  produces proportionally significantly different results in the  $C_p^g$  for the samples  
59  
222 investigated (Table 1). The maximum decrease of  $C_p^g$  observed for Etna trachybasalt, An<sub>10</sub> and An<sub>42</sub>

223 are 5, 10, and 10 J mol<sup>-1</sup> K<sup>-1</sup>, corresponding to 7%, 12%, and 14% reductions in the initial  
1  
224 anhydrous values, are due to the addition 11.4, 10.3 and 8.5 mol% H<sub>2</sub>O, respectively.

225  
226 **3.1.2. Specific heat capacity of hydrous liquids ( $C_p^l$ ) and the configurational heat capacity ( $C_p^c$ )**

227 The variation of  $C_p^l$  with H<sub>2</sub>O content in the Etna trachybasalt shows a smooth curving  
10  
228 downward pattern. Opposite to the pattern observed for  $C_p^s$ ,  $C_p^l$  decreases only slightly (from 97.9  
13  
229 to 96.3) up to 2.31 wt% (7.82 mol%) H<sub>2</sub>O, then shows a steeper decrease (from 96.3 to 92.4) from  
14  
230 2.31 to 3.46 (11.39 mol%) wt% H<sub>2</sub>O. Small effects (up to a maximum of ~ 8% for An100) are also  
16  
231 observed for samples in the An-Di system. The effect of dissolved H<sub>2</sub>O on the  $C_p^l$  values for the  
18  
232 An-Di system shows similar relationships to those observed for  $C_p^s$ , with An<sub>100</sub> and An<sub>90</sub> having  
20  
233 similar to slightly higher  $C_p^l$  values with respect to the Etna trachybasalt  $C_p^l$  values at the same H<sub>2</sub>O  
21  
234 content, while the values for An<sub>42</sub> and An<sub>10</sub> at the same H<sub>2</sub>O content are systematically lower (Table  
22  
235 1). For all investigated samples, the initial dissolution of H<sub>2</sub>O in the anhydrous melt compositions  
23  
236 produces an increase in the  $C_p^c$  values. Moreover  $C_p^c$  for the Etna trachybasalt shows a concave  
24  
237 trend as a function of H<sub>2</sub>O (Fig. 2). This trend is determined by a progressive increase of  $C_p^c$  from  
25  
238 21.6 up to 25.8 J mol<sup>-1</sup> K<sup>-1</sup>, due to the addition of 2.31 wt% H<sub>2</sub>O, followed by a sharp decrease to  
26  
239 20.9 J mol<sup>-1</sup> K<sup>-1</sup> as H<sub>2</sub>O content further increases up to 3.46 wt%. This decrease is visible only for  
27  
240 the Etna trachybasalt, maybe due to the greater amount of H<sub>2</sub>O dissolved in this liquid compared to  
28  
241 the other samples analyzed. An<sub>100</sub> contains almost the same amount of H<sub>2</sub>O as the Etna samples. In  
29  
242 detail, the maximum variation in  $C_p^c$  due to the addition of H<sub>2</sub>O is different for each dataset, from ~  
30  
243 +40% for the An<sub>10</sub> sample; +/-20% for Etna and ~ +13% for An<sub>42</sub>. Given the limited number of data  
31  
244 available, the  $C_p^c$  variations for An<sub>100</sub> and An<sub>90</sub> are more difficult to evaluate as these datasets  
32  
245 consist of only two points (Table 1).

246  
247 **3.2.  $C_p$  variations of hydrous melts and glasses with composition ( $SM_{hydrous}$ ,  $NBO/T_{hydrous}$ )**

248 In order to evaluate the effect of structure on the  $C_p$  of the investigated systems, we calculated,  
 1  
 249 for both dry and hydrous compositions, the structure modifier ( $SM$ ; Giordano et al. 2009) and the  
 3  
 250 non-bridging oxygen over tetrahedra ( $NBO/T$ ) parameters, assuming  $H_2O$  as a network modifier.  
 4  
 251 The modified  $SM$  parameter, referred to hereafter as  $SM_{hydrous}$ , is calculated, in mol%, as the sum of  
 6  
 252 the network modifier oxides plus the amount of dissolved  $H_2O$  (Giordano et al. 2009; Mercier et al.  
 10  
 253 2009), without accounting for  $H_2O$  speciation. The modified  $NBO/T$  parameter,  $NBO/T_{hydrous}$ , is  
 13  
 254 calculated assuming all hydrogen is in a network modifier role. Both the  $SM_{hydrous}$  and  $NBO/T_{hydrous}$   
 15  
 255 are considered to be representative of the degree of polymerization of the hydrous liquids (Mysen,  
 18  
 256 1988; Giordano et al. 2009). In our calculation, iron was partitioned following the principles of  
 20  
 257 Mercier et al. (2009), who assumed an average iron oxidation state ratio of 0.5 for dry samples  
 23  
 258 quenched in air. For the hydrous samples synthesized in pressure vessels the iron oxidation state  
 25  
 259 was not directly determined, and we arbitrarily chose the same average iron oxidation state ratio of  
 27  
 260 0.5. The latter value is realistic and fits with the average iron oxidation state of most of the  
 30  
 261 synthesised anhydrous glasses (Di Muro et al., 2009).  
 32

33  
 262 Figure 3 illustrates how  $C_p^g$ ,  $C_p^l$ , and  $C_p^c$  vary as a function of these parameters, in a  
 35  
 263 compositional regime encompassing more polymerized to more depolymerized glasses/liquids. By  
 37  
 264 observing the heat capacity variation in the different compositional domains of Fig. 3 ( $SM_{hydrous}$ ,  
 40  
 265  $NBO/T_{hydrous}$ ), the trends of Fig. 2 are more evident. In particular,  $C_p^l$  and  $C_p^g$  decrease smoothly as  
 42  
 266 a function of  $SM_{hydrous}$  and  $NBO/T_{hydrous}$ , with values decreasing from An<sub>100</sub> ( $SM_{hydrous}$  =26.1;  
 44  
 267  $NBO/T_{hydrous}$  = 0.04) to An<sub>90</sub> ( $SM_{hydrous}$  =31.5;  $NBO/T_{hydrous}$  = 0.25); Etna trachybasalt ( $SM_{hydrous}$  =  
 47  
 268 33;  $NBO/T_{hydrous}$  = 0.47); An<sub>42</sub> ( $SM_{hydrous}$  =39.5;  $NBO/T_{hydrous}$  = 0.83) and An<sub>10</sub> ( $SM_{hydrous}$  =45.3;  
 49  
 269  $NBO/T_{hydrous}$  = 1.50). Sample An<sub>10</sub> is somewhat anomalous as it shows a slight increase (~ 2.5% of  
 52  
 270 the measured value) of  $C_p^l$  and  $C_p^g$ , as already shown in Fig. 2b.  $C_p^c$ , on the other hand, shows a  
 54  
 271 slight increase with increasing the degree of depolymerization. These trends suggest that, for the  
 57  
 272 samples investigated here,  $C_p^g$ ,  $C_p^l$  and  $C_p^c$  can be, to a first approximation, described in terms as a  
 59  
 273 function of  $SM_{hydrous}$ ,  $NBO/T_{hydrous}$ .  
 60

274 Variations in  $C_p^l$  and  $C_p^g$  as a function of these compositional parameters define relative  
1  
275 minima at  $SM_{hydrous} \sim 45$  mol%,  $NBO/T_{hydrous} \sim 1.2$ ; a minimum is not observed in the variation of  
3  
4  
276  $C_p^c$ . In order to interpret and rationalize this behaviour, we have expanded our analysis (Fig. 4) to  
5  
6  
277 include other published data for more polymerized and depolymerized hydrous melt compositions  
7  
8  
278 (Bouhifd et al. 2006; Bouhifd et al. 2013). Data from Di Genova et al (2014) for the Etna  
9  
10  
279 trachybasalt agree well with our measurements (see Table 2) and are plotted in Fig. 4 with the same  
11  
12  
13  
280 symbols (but smaller size) as our data for Etna.  
14  
15  
16

281

18

282

20

21

283

23

284

25

285

26

286

30

31

287

32

33

288

35

36

289

37

38

290

40

291

42

43

292

44

45

293

47

48

294

49

50

295

52

53

296

54

55

297

57

58

298

59

60

299

61

62

63

64

65

## 4. Discussion

### 4.1. Heat capacity of glasses and liquids

#### 4.1.1. Comparison with previous data

Our data on hydrous iron-bearing natural trachybasalt and synthetic An-Di compositions are compared with measurements on iron-free and iron-bearing compositions that are both more polymerized (i.e., albite, phonolite, trachyte, pantellerite) (Bouhifd et al. 2006, Di Genova et al. 2014) and less polymerized (i.e., tephrite, basalt, latite, foidite) (Bouhifd et al. 2013, Di Genova et al. 2014).

Figure 4 shows how  $C_p^g$ ,  $C_p^l$  and  $C_p^c$  vary as a function of H<sub>2</sub>O (panel A) and the  $SM_{hydrous}$  parameter (panel B). Largely, it appears that polymerized melts have higher  $C_p^g$  values and lower  $C_p^l$  and  $C_p^c$  than the Etna trachybasalts and the other more depolymerized multicomponent melts. An increase in the  $SM_{hydrous}$  parameter causes the  $C_p^c$  of polymerized and depolymerized melts to increase, although its effect on depolymerized melts is significantly smaller. In general, it appears that  $C_p^c$  increases up to  $SM_{hydrous}$  of about 30 – 35 mol%, whereas any further increase in  $SM_{hydrous}$  affects  $C_p^c$  to a smaller extent. The depolymerized tephritic and foiditic samples measured by Bouhifd et al. (2013) have, apart from the samples with the highest H<sub>2</sub>O contents (Teph 2.2, NIQ 1.8),  $C_p^c$  values similar to those measured for the Etna trachybasalt and An-Di compositions (Table



1). On the contrary,  $C_p^g$ ,  $C_p^l$  of tephritic compositions (Teph, NIQ), and similarly sample An<sub>10</sub>, show a marked departure from the trends observed for the Etna trachybasalt. On the other hand, the pattern followed by  $C_p^c$  for these samples, although a bit steeper, appears to follow the overall path followed by the other compositions. Fig. 4A shows more clearly the effect of H<sub>2</sub>O has on the  $C_p$  data of more depolymerized compositions (Teph, NIQ) measured by Bouhifd et al (2013) compared to the Etna trachybasalt. It shows that, apart from the  $C_p^l$  of sample Teph 2.2, the overall effect of H<sub>2</sub>O on  $C_p$  of these depolymerized compositions is similar to, and substantially follows the same paths, as those of the Etna trachybasalt, although the  $C_p$  of these samples has only been measured at low H<sub>2</sub>O contents. It is important to note that the trend of  $C_p^l$  for the FR latite sample (Di Genova et al. 2014) apparently shows a deviation from the overall trend.

The relative minima observed in Fig 4b for  $C_p^l$  and  $C_p^g$  generated by fitting the hydrous An-Di compositions persist even after adding the data from Bouhifd et al. (2013) and Di Genova et al. (2014). The reason for the minima are unclear; they could really represent a local minimum with underlying structural reasons, but they could also be a result of peculiar behaviour of the simplified hydrous An-Di compositions, fitting limitations, or an artifact of expressing composition in terms of  $SM_{hydrous}$ ,  $NBO/T_{hydrous}$  and the molar mass parameters.

#### 4.1.2. Partial molar heat capacity of H<sub>2</sub>O of silicate glasses ( $C_p^g_{H_2O}$ ) and liquids ( $C_p^l_{H_2O}$ )

We have compared our results with previous models for anhydrous glasses (Richet, 1987) and for anhydrous liquids (Richet and Bottinga, 1985; Lange and Navrotsky, 1992; Stebbins et al. 1984). We have modified these models to account for the effects of H<sub>2</sub>O (using the partial molar heat capacity of H<sub>2</sub>O in silicate glasses,  $C_p^g_{H_2O}$ , and liquids,  $C_p^l_{H_2O}$ ) using the approach of Bouhifd et al. (2006; 2013) and Di Genova et al. (2014).

In general, the Richet (1987) model shows that the heat capacity of the glasses can be predicted by the following additive function of composition:

$$C_p^g = \sum x_i C_p^g i(T) \quad (1)$$

326 where  $x_i$  is the mole fraction of oxide and  $C_p^{g_i}$  is the partial molar heat capacity of oxide  $i$  in the  
1  
327 glass which depends on temperature (Richet, 1987).

328 Measured and calculated  $C_p^g$  for anhydrous and hydrous glasses are within error of the values  
3  
4  
5  
6  
329 expected using the model. Given the fact that the Richet (1987) glass model is calibrated on a  
7  
8  
9  
330 database significantly larger than that of our study, we assume that it provides the most accurate  
10  
11  
12  
331 estimates of  $C_p^{g_i}$  for anhydrous glasses available so far. For hydrous glasses we assume that the  
13  
14  
15  
332 temperature dependence of  $C_p^{g_{H_2O}}$  is well represented by the equation obtained by Bouhifd et al.  
16  
17  
333 (2006), which assumes it is independent of composition.

18  
19  
334 The  $C_p^l$  measured here and in the previous work by Bouhifd et al. (2006; 2013) for hydrous  
20  
21  
22  
335 compositions have been compared with predictions made using the models for anhydrous  
23  
24  
25  
336 compositions from Stebbins et al. (1984), Richet and Bottinga (1985), implemented for the  
26  
27  
337 temperature dependent partial molar heat capacity of  $Al_2O_3$  as obtained by Courtial and Richet  
28  
29  
338 (1993), and Lange and Navrotsky (1992). In the subsequent discussion these models will be referred  
30  
31  
339 to as S`84, RBC`85,93 and LN`92, respectively. We have also compared the measured  $C_p^l$  with  
32  
33  
340 those predicted using  $C_p^{l_{H_2O}}$  obtained by Bouhifd et al. (2006; 2013) combined with the above  
34  
35  
36  
341 mentioned S`84, RBC`85,93 and LN`92 models. In our calculation, iron was partitioned following  
37  
38  
39  
342 the principles of Mercier et al. (2009), who assumed an average iron oxidation state ratio of 0.5 for  
40  
41  
42  
343 dry samples quenched in air. For the hydrous samples synthesized in pressure vessels the iron  
43  
44  
344 oxidation state was not directly determined, and we arbitrarily chose the same average iron  
45  
46  
47  
345 oxidation state ratio of 0.5. Nonetheless, the heating cycles that each sample has gone will remove  
48  
49  
346 the thermal history that the sample experienced during its synthesis, resulting in sample  
50  
51  
347 equilibration at pressure conditions similar to atmospheric under argon flow to prevent oxidation.

52  
53  
348 Table 1 shows the predicted  $C_p^l$  values using the S`84, RBC`85,93 and LN`92 models. The  
54  
55  
349 calculations were performed using the  $C_p^{l_{H_2O}}$  of  $85 \text{ J mol}^{-1} \text{ K}^{-1}$ , proposed by Bouhifd et al. (2006),  
56  
57  
58  
350 the  $C_p^{l_{H_2O}}$  of  $237 \text{ J mol}^{-1} \text{ K}^{-1}$  estimated by Bouhifd et al. (2013) and the  $C_p^{l_{H_2O}}$  of  $41 \text{ J mol}^{-1} \text{ K}^{-1}$   
59  
60  
351 estimated by Di Genova et al. (2014).

352 Our parameterization based on the data compiled here (Table 1) and based on the  
1  
353 minimization of standard deviation and relative errors suggests an optimal value for  $C_p^l_{H2O}$  of 79 J  
3  
354  $\text{mol}^{-1} \text{K}^{-1}$ . This value is in close agreement with the early studies of Burnham and Davis (1974) and  
4  
5  
6  
355 Clemens and Navrotsky (1987) and provides a better fit to the data than other values (e.g., Table 1).  
8

356 In particular, the  $C_p^l_{H2O}$  of 79 J  $\text{mol}^{-1}\text{K}^{-1}$  reduces the deviation from model calculations to  
9  
10  
11  
12  
357 1.6%.  $T_g^{liquid}$  used to calculate  $C_p^l$  by the RBC`85,93 model are reported in Table 1.  
13

14  
15  
358 If instead all the data measured in this study and the Bouhifd et al. (2006, 2013) studies are  
16  
17  
359 considered, the RBC`85,93 and S`84 models using either the  $C_p^l_{H2O}$  defined here (79 J/mol\*K) or  
18  
19  
20  
360 by Bouhifd et al. (2006) (85 J/mol\*K), reproduce the data equally well. Results using both the  
21  
22  
361 RBC`85,93 and S`84 models are based on the minimization of the average relative error (3.7%). In  
23  
24  
25  
362 particular, the  $C_p^l$  measured in this work are best reproduced by the RBC`85,93 model (to within  
26  
27  
363 1.1% and 1.9 % relative error for the Etna trachybasalt and the Anorthite-Diopside join). The largest  
28  
29  
30  
364 difference between the measured and predicted values is observed for the Teph 2.2 liquid measured  
31  
32  
365 by Bouhifd et al. (2013) (Table 1).  
33

366 If we consider single datasets, the data obtained in this study are better described by the  
34  
35  
367 RBC`85,93 model. On the other hand, this is not true if we include in our analysis the data from  
36  
37  
368 Bouhifd et al (2006, 2013). In this case, the phonolitic and trachytic compositions investigated by  
38  
39  
40  
369 Bouhifd et al (2006) are better reproduced by the LN '92 model, whereas the albitic liquid is best  
41  
42  
43  
370 reproduced by the S '84 model. Finally, the tephritic and foiditic compositions are better reproduced  
44  
45  
46  
371 by the S'84 model. In every case it did not matter whether the  $C_p^l_{H2O}$  defined in this study or that  
47  
48  
49  
372 defined by Bouhifd et al. (2006) was used.

#### 50 373 4.1.3. Relationships between $T_g^{onset}$ , $T_g^{liquid}$ and $T_g^{12}$ 52

53  
54  
374 Figure 5A compares  $T_g^{onset}$  with  $T_g^{liquid}$  and includes data presented here and from Giordano et  
55  
56  
375 al. (2005; 2008) and Bouhifd et al. (2006; 2013).  $T_g^{onset}$  with  $T_g^{liquid}$  show a strong positive  
57  
58  
59  
376 correlation with a slope of 1 and an intercept value of ~58 K, which represents the average  $\Delta T$  over  
60  
61  
377 which the glass to melt transition is measured. To a first approximation the correlation between  
62  
63  
64  
65

378  $T_g^{onset}$  and  $T_g^{liquid}$  is clearly independent of composition and H<sub>2</sub>O content (Giordano et al. 2005,  
 1  
 379 2008). We have also plotted the calorimetrically measured values of  $T_g^{onset}$  against model values of  
 3  
 380  $T_g^{12}$ , the glass transition temperature, as calculated from Adam Gibbs model values at viscosity of  
 4  
 381  $10^{12}$  Pa s (see § 4.2; Table 2) in Fig. 5B. There is clear agreement (see Appendix) between the  
 6  
 382 calorimetric (observed) and predicted (modeled) glass transition temperatures.  
 8  
 9

10  
 11  
 12  
 13  
 14  
 15

## 384 **4.2. Configurational contribution**

### 385 *4.2.1. Relationship with the viscosity of silicate melts*

18  
 19  
 20  
 21  
 22  
 23  
 24  
 25  
 26  
 27  
 28  
 29  
 30  
 31  
 32  
 33  
 34  
 35  
 36  
 37  
 38  
 39  
 40  
 41  
 42  
 43  
 44  
 45  
 46  
 47  
 48  
 49  
 50  
 51  
 52  
 53  
 54  
 55  
 56  
 57  
 58  
 59  
 60  
 61  
 62  
 63  
 64  
 65

The capacity of liquids to adopt different structural configurations as a function of temperature distinguishes them from solids. Indeed, the difference in heat capacity between a glass and the corresponding fully relaxed liquid at the limiting fictive temperature is a direct record of these configurational changes. Classically, it is referred to as the configurational heat capacity  $C_p^c$  and there is a corresponding configurational entropy ( $S^c$ ) (the same as macroscopic entropy) that is functionally dependent on  $C_p^c$  (e.g. Richet, 1987; Richet and Bottinga, 1985, 1995 and Toplis et al. 2001). These thermochemical properties (i.e.  $S^c$  and  $C_p^c$ ) reflect the changes in structural state of the melt as it transitions to a glass, and the Adam and Gibbs theory (Adam and Gibbs, 1965) provides a connection to the temperature dependence of melt viscosity by:

$$\log \eta = A_{AG} + B_{AG} / (T S^c(T)) \quad (2)$$

The variables include the pre-exponential term  $A_{AG}$ , the potential energy barrier hindering the structural rearrangement of the liquid  $B_{AG}$ , and the configurational entropy of the liquid at a temperature of interest ( $S^c(T)$ ). The variable  $S^c(T)$  represents a measure of the number of configurations accessible to the liquid and can be related to the configurational energies at the glass transition temperature ( $T_g$ ) by the expansion:

$$S^c(T) = S^c(T_g) + \int_{T_g}^T (C_p^c / T) dT \quad (3)$$

We have used the complementary viscosity data available for the melts listed in Table 2 to obtain model estimates of  $S^c(T_g)$ . We mainly follow the work of Richet (1984), Toplis et al. (1997),

404 Toplis (1998) and Webb (2008), wherein Eq. 1 is fitted to measurements of  $C_p^c$  and melt viscosity  
1  
405 for the same melt compositions (Giordano et al. 2005, 2008; Whittington et al. 2000, 2001) and the  
3  
406 adjustable parameters are  $A_{AG}$ ,  $B_{AG}$  and  $S^c(T_g)$ . A full description of our optimization philosophy and  
4  
6  
407 methodology is provided in the Appendix where we remodel a subset of the data analyzed by Toplis  
8  
408 et al. (1997). The main and most important difference in our approach is that we assume that  $A_{AG}$ ,  
10  
409 the pre-exponential term in Eq. 1, is a constant for all melts. The variable  $A$ , in most conventional  
11  
13  
410 equations describing the temperature dependence of melt viscosity, represents the high temperature  
14  
15  
411 limits to viscosity. This value has been shown theoretically and empirically to be a constant value  
16  
18  
412 for all silicate melts and, thus, independent of composition by Russell et al. (2002; 2003), Russell  
19  
20  
413 and Giordano (2005), Giordano and Russell (2007) and Giordano et al. (2008b).21  
22  
23

414         Operationally we combined all datasets ( $k=23$ ) comprising measured values of  $C_p^c$ , onset  
24  
25  
415 values of  $T_g$ , and melt viscosity measurements at four or more temperatures to create a single  
26  
27  
28  
416 overdetermined system of non-linear equations ( $n=292$ ). The adjustable parameters included: a  
29  
30  
417 single common unknown value of  $A_{AG}$  and  $k$  values of  $B_{AG}$  and  $S^c(T_g)$ , each ( $2*k+1 = 47$ ). We then  
31  
32  
33  
418 applied the optimal value of  $A_{AG}$  (-3.51) to model the other melt compositions that had fewer than  
34  
35  
419 four temperature measurements of viscosity ( $k' = 18$ ; Table 2). Specifically, we fitted Eq. 1 to the  
36  
37  
38  
420 data available for individual melt compositions assuming that  $A_{AG} = -3.51$  to retrieve optimal values  
39  
40  
421 of  $B_{AG}$  and  $S^c(T_g)$  for these melts. This two-pronged modeling strategy put all model parameters on  
41  
42  
43  
422 the same platform (e.g., a common value of  $A$  for the high temperature viscosity limit) and thereby,  
44  
45  
423 avoided problems that arise from using an arbitrary value of  $A_{AG}$ , (cf. Toplis et al. 1997; Webb  
46  
47  
48  
424 2008).49

50  
51  
52  
53  
54  
55  
56  
57  
58  
59  
60  
61  
62  
63  
64  
65

The results of our optimization for best fit values of  $A_{AG}$ ,  $B_{AG}$  and  $S^c(T_g)$  are illustrated in  
Figure 6A. Our model reproduces the original viscosity data to within measurement error (Fig. 6B).  
The range of model values of  $B_{AG}$  and  $S^c(T_g)$  for a fixed value of  $A_{AG}$  of -3.51 is shown in Fig. 6A;  
 $S^c(T_g)$  varies from 9 - 35 J mol<sup>-1</sup> K<sup>-1</sup> whilst  $B_{AG}$  ranges from 150 - 450 kJ mol<sup>-1</sup>. The two parameters  
show a very strong positive correlation and part of this is a model-induced covariation (cf.

430 Appendix A; Russell et al. 2002). However, the range of values in Fig. 6A span a range much larger  
 1  
 431 than the confidence ellipses arising from analytical uncertainties and the functional form of the  
 3  
 432 equation, indicating that  $A_{AG}$  and  $B_{AG}$  are, in fact, positively correlated properties of these melts.  
 4  
 5  
 6

433 We have also discriminated the anhydrous (black symbols) from the hydrous (grey) melts  
 8  
 434 and used the size of symbol to indicate the relative H<sub>2</sub>O contents. Values of  $B_{AG}$  and  $S^c(T_g)$  for the  
 10  
 11 anhydrous melts are uniformly lower than for the H<sub>2</sub>O-bearing melts. However, there is no single  
 12  
 13  
 14  
 435 systematic pattern in  $B_{AG}$  and  $S^c(T_g)$  values with increasing amounts of H<sub>2</sub>O suggesting that the  
 15  
 16 parameters are controlled by both melt composition and H<sub>2</sub>O content, although the highest H<sub>2</sub>O  
 17  
 18 contents do suggest a decrease in values of  $B_{AG}$ .  
 19  
 20

21  
 439 On the basis of our model optimization we have calculated the derivative transport  
 22  
 23 properties  $T_g^{12}$  and melt fragility ( $m$ ). As developed by Toplis et al. (1997), these properties can be  
 24  
 25  
 26  
 441 computed for each melt from the measured values of  $C_p^c$  and the model values of  $A_{AG}$ ,  $B_{AG}$  and  
 27  
 28  
 442  $S^c(T_g)$ :  
 29  
 30

$$443 \quad T_g^{12} = \frac{B_{AG}}{(12 \ A_{AG}) S^c(T_g)} \quad (4)$$

35  
 444 and  
 36

$$445 \quad m = [12 \ A_{AG}] \left( 1 + \frac{C_p^c}{S^c(T_g)} \right) \quad (5)$$

37  
 38  
 446 respectively. The calculated values of  $T_g^{12}$  and fragility for the suite of 31 anhydrous (black  
 43  
 44 symbols) and hydrous (grey symbols) melts are plotted in Figure 6C. The dataset describes a  
 45  
 46  
 47  
 448 general trend that echoes the pattern predicted by the Giordano et al. (2008) viscosity model (cf.  
 48  
 49  
 449 Fig. 6b in Giordano et al. 2008). The anhydrous melts show a range of fragilities 25-60 and a  
 51  
 52  
 450 narrow range of model values of  $T_g^{12}$  (900-1150 K). The addition of H<sub>2</sub>O causes a pronounced  
 53  
 54  
 451 decrease in  $T_g^{12}$  values (600-900K) and has variable effects on melt fragility; although the reduced  
 55  
 56  
 452 range of fragilities (20-45) for hydrous melts suggests that dissolved H<sub>2</sub>O causes many melts to  
 57  
 58  
 453 become more Arrhenian-like and stronger (Giordano et al. 2008b; 2009). These results are partially  
 59  
 60

454 corroborated by Di Genova et al. (2014) who noticed that the effect of H<sub>2</sub>O on fragility depends on  
1  
455 the degree of polymerization of the anhydrous equivalent melt.  
3

456 The addition of dissolved H<sub>2</sub>O, on the order of 3 wt%, causes a marked increase (up to  
4  
5  
6  
457 three-fold) in  $B_{AG}$  and  $S^c(T_g)$  values for the An-Di and Etna melts, as well as, the more  
8  
9  
458 depolymerized compositions of Bouhifd et al (2013). A similar, but significantly less marked  
10  
11  
459 increase is observed for the more polymerized melts of Bouhifd et al. (2006). In this case  $B_{AG}$   
13  
14  
460 increases only slightly whilst  $S^c(T_g)$  increases to nearly double the anhydrous value.  
15

461 Figure 7 shows how the ratio  $B_{AG}/S^c(T_g)$  varies as a function of H<sub>2</sub>O and  $SM_{hydrous}$  and  
16  
17  
462 provides a means to explain, according to Eq. 1, the low viscosity of hydrous Etna trachybasalt  
18  
19  
20  
463 relative to the An-Di-H<sub>2</sub>O system. As H<sub>2</sub>O content increases, in fact, the Etna trachybasalt shows  
21  
22  
23  
464 the lowest  $B_{AG}/S^c(T_g)$  values and consequently the lowest viscosity at the same H<sub>2</sub>O (Fig 7A).  
25

465 Fig. 7B shows how the  $B_{AG}/S^c(T_g)$  ratio varies as a function of the  $SM_{hydrous}$  parameter which  
26  
27  
28  
466 largely represents the degree of polymerization. In the glass transition interval (where  $S^c(T) \simeq$   
29  
30  
467  $S^c(T_g)$ ), the variation of the  $B_{AG}/S^c(T_g)$  ratio largely follows (Eq. 1) the path of viscosity variation,  
31  
32  
33  
468 meaning that, in that interval, lower  $B_{AG}/S^c(T_g)$  values correspond to lower viscosities. Accordingly  
34  
35  
469 Fig. 7 shows the reason that the Etna trachybasalt has a viscosity lower than An-Di melts in the  
36  
37  
38  
470 glass transition interval. The figure also suggests that higher  $SM_{hydrous}$  values do not guarantee lower  
39  
40  
41  
471 viscosity. An-Di melts, commonly considered highly depolymerized melts, have neither the lowest  
42  
43  
472  $B_{AG}/S^c(T_g)$  ratios nor the lowest viscosities.  
44

473 The key to understanding the differences in behaviour between the multicomponent Etna  
45  
46  
47  
48  
474 compositions and the melts in the An-Di system resides in understanding the role of iron in the  
49  
50  
51  
475 structure and thermodynamic quantities of natural silicate melts (Chevrel et al. 2013).  
52

### 476 4.3. Structural considerations 53 54 55 56

57  
58  
478 For both dry and hydrous compositions, the variation in  $C_p^g$  observed among the different  
59  
60  
479 liquids are related to vibrational contributions, directly linked to the cation field strength, of  
61

480 chemical bonds in the structure (Giordano et al. 2008a, 2009). Therefore intuitively more  
1  
481 depolymerised glasses will have longer and weaker Tetrahedra-Oxygen (TO) bonds associated with  
3  
482 lower values of  $C_p^g$ . The trends visible in Fig. 3 and 4 are in perfect agreement with this  
4  
5  
6  
483 consideration.

484 Trends in  $C_p^c$  can be discussed in more detail. In general,  $C_p^c$  is defined as the energy needed  
10  
11  
485 to change the structure of a liquid in response to temperature variations across the glass transition  
12  
13  
486 and it is made of a chemical and a topological contribution. The chemical contribution has to do  
14  
15  
487 with mixing of various chemical component in the silicate framework, (Al/Si order disorder, mixing  
16  
17  
488 of cationic sites, Q species equilibria triclusters, ion channeling, bond dangling, coordination state  
18  
19  
489 of network formers, coordination changes of network modifiers, etc. see Stebbins, 2008; Giordano  
20  
21  
22  
23  
490 et al. 2008a), whereas the topological contribution is related to the framework of the silicate  
24  
25  
491 network, therefore the configuration of the oxygen matrix, expressed in terms of TO bonds and  
26  
27  
28  
492 TOT angle distribution.

493 It has previously been observed (Richet and Bottinga, 1985; Bouhfid et al. 1998; Toplis et al.  
31  
32  
33  
494 2001; Webb, 2008; Di Genova et al., 2014) that  $C_p^c$  increases with decreasing SiO<sub>2</sub>. In general, this  
34  
35  
495 increase is ascribed to a decrease in the overall strength of TO bonds and to a correlated increase of  
36  
37  
38  
496 the TO and TOT distribution (topological contribution to the configurational heat capacity). Second  
39  
40  
497 order variation in the  $C_p^c$ , at similar  $NBO/T_{hydrous}$  or  $SM_{hydrous}$  values, can be due to different Al/Si  
41  
42  
43  
498 and/or alkali versus alkaline earth ratios.

499 The results shown in Fig. 4 are consistent with the increase in  $C_p^c$  as a function of the degree  
47  
48  
500 of depolymerisation of the melt that accompanies the decrease in SiO<sub>2</sub>. The leveling off of  $C_p^c$  at  
49  
50  
501  $SM_{hydrous} \sim 30\text{-}35\text{ mol}\%$  ( $NBO/T_{hydrous} \sim 0.5$ ) is more intriguing as it suggests that after a certain  
51  
52  
502 degree of depolymerisation, pertaining approximately to basaltic compositions, further increase in  
53  
54  
503 depolymerisation does not translate into a perceivable increase in the configurational heat capacity  
55  
56  
57  
504 (or decrease in viscosity), as the increase in disorder (chemical or topological) does not have any  
58  
59  
60  
61  
505 appreciable effect on the energetics of an already extremely disordered/depolymerized liquid



506 (Giordano et al. 2008a). One possibility is that the observed leveling could be driven by stabilizing  
1  
507 Al in lower coordination state (i.e., in Al<sup>[4]</sup> by alkalis or alkaline earth elements until the  
3  
508 peraluminous melts become metaluminous (i.e., charge balanced)) and then further in peralkaline or  
4  
509 peralkaline-earth field where Al starts to have higher coordination (C<sub>N</sub>) and forming NBO on Si (Si-  
6  
510 O-Al).  
8  
9

11 The introduction of H<sub>2</sub>O in the silicate liquids seems to largely mimic the behavior of the  
12 other oxides (Fig 3 and 4).  $C_p^c$  seems to steadily increase as a function of H<sub>2</sub>O content for  
13 polymerized compositions ( $SM_{hydrous}$  ~30-35 in Fig. 4), whereas, for more depolymerized liquids  
14 ( $SM_{hydrous}$  >30-35) it tends to level off and not to be affected by the introduction of H<sub>2</sub>O (Fig. 2) or  
15 others oxides (Fig. 4). This general trend seems not to include An<sub>10</sub> composition and the tephritic  
16 and NIQ compositions from Bouhifd (2013), which instead display a small but distinctive increase  
17 of  $C_p^c$  as H<sub>2</sub>O is introduced into the liquid. In contrast, the Etna compositions display the opposite  
18 behavior with a small increase in  $C_p^c$  upon introduction of H<sub>2</sub>O. The limited number of calorimetric  
19 data for hydrous melts and, in particular, on melts having very high H<sub>2</sub>O contents (e.g., >10 mol %)   
20 precludes an unambiguous interpretation of this behavior.  
21  
22  
23  
24  
25  
26  
27  
28  
29  
30  
31  
32  
33  
34  
35

36 In deriving  $SM_{hydrous}$  and  $NBO/T_{hydrous}$  parameters, we consider total H<sub>2</sub>O to be a network  
37 modifier without accounting for water speciation, therefore possibly overestimating the extent of  
38 H<sub>2</sub>O in a network modifier role. Speciation of water and the different structural role of molecular  
39 versus hydroxyl groups are therefore fundamental to specifically address this issue. Moreover, the  
40 presence of H<sub>2</sub>O may influence the oxidation state of iron (Fe<sup>2+</sup>/Fe<sup>3+</sup>) affecting the calculation of the  
41 considered polymerization parameter, which in this case have been set on the basis of the structural  
42 considerations provided by Mercier et al. (2009) to Fe<sup>2+</sup>/Fe<sup>3+</sup> = 0.5.  
43  
44  
45  
46  
47  
48  
49  
50  
51  
52

53 In summary whereas general trends can be envisaged in both  $C_p^c$  and  $C_p^s$  as a function of  
54 chemical compositions and degree of depolymerization, further data exploring the complexity of  
55 natural melts is required in the future to validate and generalize our modeling and interpretation. At  
56 present, there are insufficient experimental data to model the effect of iron redox on the heat  
57  
58  
59  
60  
61  
62  
63  
64  
65

532 capacities of multicomponent silicate melts, so also in this case, further studies will be needed to  
1  
533 investigate this aspect more in details. Finally, our approach is strictly empirical; the chemical  
3  
534 components we have chosen have no explicit or independent relationship to the structure or  
6  
535 speciation of the silicate melt. We believe that future models may benefit immensely from a  
8  
536 calibration based on a component basis that, at least in part, reflects melt speciation.  
10

## 538 5. Conclusions.

539 The results of this investigation show that:

- 540 1) the  $C_p$  of polymerized and depolymerized compositions are different and can be largely  
20 distinguished in terms of compositional parameters accounting for the modifying effect of  
21  
22 H<sub>2</sub>O in the structure (e.g.,  $SM_{hydrous}$  or NBO/T);  
25
- 543 2) a compositional dependence of the partial molar heat capacity of H<sub>2</sub>O for both glasses and  
27 liquids has not been observed;  
28
- 544 3) we estimate an optimal  $C_p^{l_{H_2O}}$  of 79 J mol<sup>-1</sup> K<sup>-1</sup>;  
30
- 545 4) our value for  $C_p^{l_{H_2O}}$  used in conjunction with existing predictive models for anhydrous melts  
32  
33  
546 can reproduce measured  $C_p$  values for hydrous glasses and liquids to within 3% relative  
35  
36  
37 error;  
38
- 548 5) the Adam-Gibbs equation fitted to a large dataset comprising the corresponding  
40  
549 measurements of melt viscosity constrains the high temperature limits of melt viscosity  
42  
550 10<sup>-3.5</sup> Pa s and provides estimates of  $B_{AG}$  and  $S_{AG}^c$ ;  
43  
44
- 551 6) values of  $B_{AG}$  and  $S_{AG}^c$  strongly reflect the degree of polymerization of the melts and are  
47  
48  
552 strongly affected by H<sub>2</sub>O content of the melt.  
49  
50  
553

554 It is possible that the absence of a distinct temperature or compositional dependence of  $C_p^{l_{H_2O}}$   
54  
55  
555 observed in our study could indeed reflect an incomplete sampling of the wide range of chemical  
57  
556 composition pertaining to natural systems. Apart from Etna trachybasalt, all the data shown in Fig 4  
59  
557 derive from simplified synthetic systems. It should also be noted that none of the models presented  
60

558 here account for the partitioning of H<sub>2</sub>O species into the silicate liquids or for their possible  
1  
559 interactions with the other oxide components. In addition, we have treated iron as a single species  
3  
560 (FeO<sub>tot</sub>), whereas silicate melts contain both ferric and ferrous iron and their proportions, which can  
4  
6  
561 vary according to temperature, composition and H<sub>2</sub>O content, and can substantially affect the  
8  
9  
562 structure of the melt (Mysen, 1988; Dingwell, 1991), but probably not their physical properties  
10  
11  
563 (Chevrel et al. 2013).

14  
564 Finally, we believe that new models should be recalibrated using measurements obtained on  
15  
16  
565 multicomponent anhydrous and hydrous liquids that consider how H<sub>2</sub>O species partition into the  
18  
19  
566 melt structure, how H<sub>2</sub>O species interact with other oxide components, and the redox state of iron.  
20

### 21 567 **Acknowledgments.**

23  
24  
568 The authors would like to knowledge two anonymous reviewers for constructive comments  
25  
569 that have led to clarification of the initial manuscript. JKR acknowledges financial support for this  
26  
570 research from grants awarded through the NSERC Discovery and Discovery Accelerator  
27  
571 Supplements programs.  
28

### 31 32 33 574 575 **References**

- 35  
576 Adam G, Gibbs JH (1965) On the temperature dependence of cooperative relaxation properties in  
37  
577 glass-forming liquids. *J Chem Phys* 43,139–146  
38  
39  
578 Avramov I (2013) The role of entropy on viscosity of silicates. *J Non-Crystalline Solids* 362:120-  
40  
579 123.  
42  
580 Behrens H, Romano C, Nowak M, Holtz F, Dingwell DB (1996) Near infrared spectroscopic  
44  
581 determination of H<sub>2</sub>O species in glasses of the system MA<sub>2</sub>Si<sub>3</sub>O<sub>8</sub> (M = Li, Na, K): an  
46  
582 interlaboratory study. *Chem Geol* 128, 41-63;  
48  
583 Behrens H, A Stuke (2003) Quantification of H<sub>2</sub>O contents in silicate glasses using IR  
49  
584 spectroscopy-a calibration based on hydrous glasses analyzed by Karl-Fisher titration *Glass*  
51  
585 *Sci. Tech.* 76, 176-189;  
53  
586 Bouhifd MA, Whittington A, Roux J, Richet P (2006) Effect of H<sub>2</sub>O on the heat capacity of  
55  
587 polymerized aluminosilicate glasses and melts. *Geochim Cosmochim Acta* 70, 711–722;  
57  
588 Bouhifd MA, Whittington A, Withers AC, Richet P (2013) Heat capacities of hydrous silicate  
58  
589 glasses and liquids *Chem Geol* 346, 125 - 134;  
60

- 590 Bowen NL (1915) The crystallization of haplobasaltic, haplodioritic and related magmas *Am J Sci*  
591 40, 161-185;
- 592 Burnham CW, Davis NF (1974) The role of H<sub>2</sub>O in silicate melts: II Thermodynamic and phase  
593 relations in the system NaAlSi<sub>3</sub>O<sub>8</sub> - H<sub>2</sub>O to 10 kilobars, 700 - 1000 °C *Am Jour Sci* 274, 902 -  
594 940;
- 595 Chevrel MO, Giordano D, Potuzak M, Courtial P, Dingwell DB (2013) Physical properties of  
596 CaAl<sub>2</sub>Si<sub>2</sub>O<sub>8</sub> - CaMgSi<sub>2</sub>O<sub>6</sub> - FeO - Fe<sub>2</sub>O<sub>3</sub> melts: Analogues for extra-terrestrial basalt *Chem*  
597 *Geol* 346, 93 - 105;
- 598 Clemens JD, Navrotsky A (1987) Mixing properties of NaAlSi<sub>3</sub>O<sub>8</sub> melt-H<sub>2</sub>O: new calorimetric data  
599 and some geological implications *J Geology* 95, 173 - 186;
- 600 Courtial P, Richet P (1993) Heat capacity of magnesium aluminosilicate melts *Geochim*  
601 *Cosmochim Acta* 57, 1267–1275;
- 602 Di Genova D, Romano C, Giordano D, Alletti M (2014) Heat capacity, configurational heat  
603 capacity and fragility of hydrous magmas *Geochim Cosmochim Acta* 142, 314 - 333;
- 604 Di Muro A, Metrich N, Mercier M, Giordano D, Massarre D, Montagnac G (2009). MicroRaman  
605 Determination of Iron Redox State in Dry Natural Glasses: Application to Peralkaline  
606 Rhyolites and Basalts. *Chem. Geol.*, 259, 78-88;
- 607 Dingwell DB (1991) Redox viscometry of some Fe-bearing silicate melts *Am Mineral* 76, 1560–  
608 1562;
- 609 Fulcher GS (1925) Analysis of recent measurements of the viscosity of glasses *Am Ceramic Soc J*  
610 8:339-355
- 611 Ghiorso MS, Sack RO (1995) Chemical mass transfer in magmatic processes: IV A revised and  
612 internally consistent thermodynamic model for the interpolation and extrapolation of liquid-  
613 solid equilibria in magmatic systems at elevated temperature and pressures *Contrib Mineral*  
614 *Petrol.* 119, 197-212.
- 615 Giordano D, Dingwell DB (2003) Viscosity of hydrous Etna basalt: implications for Plinian-style  
616 basaltic eruptions *Bull Volcanol* 65, 8-14;
- 617 Giordano D, Nichols, ARL, Dingwell DB (2005) Glass transition temperatures of natural hydrous  
618 melts: a relationship with shear viscosity and implications for the welding process *J Volcanol*  
619 *Geoth Res* 142, 105–118;
- 620 Giordano D, Russell JK (2007) A rheological model for glassforming silicate melts in the systems  
621 CAS, MAS, MCAS *J Phys Cond Matter* 19, 205148

- 622 Giordano D, Potuzak M, Romano C, Dingwell DB, Nowak M (2008a) Viscosity and glass  
623 transition temperature of hydrous melts in the system  $\text{CaAl}_2\text{Si}_2\text{O}_8$  -  $\text{CaMgSi}_2\text{O}_6$  Chem Geol  
624 256, 203-215;
- 625 Giordano D, Russell J.K, Dingwell DB (2008b) Viscosity of magmatic liquids: A model Earth  
626 Planet Sci Lett 271, 123-134
- 627 Giordano D, Ardia P, Romano C, Dingwell DB, Di Muro A, Schmidt MW, Mangiacapra A, Hess  
628 KU (2009) The rheological evolution of alkaline Vesuvius magmas and comparison with  
629 alkaline series from the Phlegrean Fields, Etna, Stromboli and Teide Geochim Cosmochim  
630 Acta 73, 6613–6630;
- 631 Kress VC, Carmichael ISE (1991) The compressibility of silicate liquids containing  $\text{Fe}_2\text{O}_3$  and the  
632 effect of composition, temperature oxygen fugacity and pressure on their redox states Contrib  
633 Mineral Petrol 108, 82–92;
- 634 Knoche R (1993) Temperaturabhängige Eigenschaften silikatischer Schmelzen Untersuchungen in  
635 den Systemen  $\text{Na}_2\text{O-SiO}_2$  und  $\text{NaAlSi}_3\text{O}_8$  -  $\text{CaAl}_2\text{Si}_2\text{O}_8$  -  $\text{CaMgSi}_2\text{O}_6$  Dissertation, Universität  
636 Bayreuth 186 pp;
- 637 Kushiro I (1973) The system diopside-anorthite-albite: determination of compositions of coexisting  
638 phases Carnegie Inst Washington Year book 72, 502-507;
- 639 Lange RA, Navrotsky A (1992) Mineralogy and Heat capacities of  $\text{Fe}_2\text{O}_3$ -bearing silicate liquids  
640 Contrib Mineral Petrol 110, 311 - 320;
- 641 Maier CG, Kelley KK (1932) An equation for the representation of high temperature heat content  
642 data J Am Ceramic Soc 54, 3243-3345;
- 643 Mercier M, Muro A D, Giordano D, Metrich N, Lesne P, Pichavant M, Scaillet B, Clocchiatti R,  
644 Montagnac G (2009) Influence of glass polymerization and oxidation on micro-Raman  $\text{H}_2\text{O}$   
645 analysis in alumino-silicate glasses Geochim Cosmochim Acta 73, 197–217;
- 646 Moynihan CT (1995) Structural relaxation in the glass transition In: Stebbins J.F, McMillan P.F,  
647 Dingwell D.B (Eds), Structure, Dynamics and Properties of Silicate Melts Reviews in  
648 Mineralogy, 32, Mineralogical Society of America, Washington, D.C, pp 1-19;
- 649 Mysen BO (1988) Structure and properties of Silicate Melts Elsevier Publishing Company,  
650 Amsterdam;
- 651 Navrotsky A, Hon R, Weill DF, Henry DJ (1980) Thermochemistry of glasses and liquids in the  
652 system  $\text{CaMgSi}_2\text{O}_6$  -  $\text{CaAl}_2\text{Si}_2\text{O}_8$  -  $\text{NaAlSi}_3\text{O}_8$ ,  $\text{SiO}_2$ - $\text{CaAl}_2\text{Si}_2\text{O}_8$ - $\text{NaAlSi}_3\text{O}_8$  and  $\text{SiO}_2$ - $\text{Al}_2\text{O}_3$ -  
653  $\text{CaO-Na}_2\text{O}$  Geochim Cosmochim Acta 44, 1409-1423;
- 654 Navrotsky A (1995) Energetics of Silicate Melts Rev Mineral 32, 121-143;

- 655 Perugini D, Poli G (2005) Viscous Fingering During Replenishment of Felsic Magma Chambers by  
656 Continuous Inputs of Mafic Magmas: Field Evidence and Fluid-Mechanics Experiments,  
657 *Geology* 33, 5-8.
- 658 Potuzak M, Nichols ARL, Dingwell DB, Clague DA (2008) Hyperquenched volcanic glass from  
659 Loihi Seamount, Hawaii, *Earth and Planetary Science Letters* 270 (1), 54-62
- 660 Pyle DM (1995) Mass and energy budgets of explosive volcanic eruptions *Geophys Res Lett* 22,  
661 563-566;
- 662 Press WH, Flannery BP, Teukolsky SA, Vetterling WT (1986) *Numerical Recipes: the Art of*  
663 *Scientific Computing* Cambridge University Press, Cambridge, 818 p.
- 664 Richet P (1987) Heat capacity of silicate glasses *Chem Geol* 62, 111–124;
- 665 Richet P (1984) Viscosity and configurational entropy of silicate melts: *Geochim Cosmochim Acta*  
666 48, 471–483;
- 667 Richet P, Bottinga Y (1985) Heat capacity of aluminum-free liquid silicates *Geochim Cosmochim*  
668 *Acta* 49, 471–486;
- 669 Richet P, Neuville DR (1992) Thermodynamics of silicate melts: Configurational properties In (Ed  
670 S Saxena) *Advances in Physical Geochemistry* 10:132-161
- 671 Richet P, Bottinga Y (1995) Rheology and Configurational Entropy of Silicate Melts In *Structure,*  
672 *Dynamics and Properties of Silicate Melts,* (Eds J.F Stebbins, P.F McMillan and Dingwell  
673 DB), *Rev Mineral* 32, 67-94;
- 674 Russell JK (1990) Magma Mixing Processes: Insights and constraints from thermodynamics  
675 calculations In *Modern Methods of Igneous Petrology: Understanding Magmatic Processes*  
676 (Eds J Nicholls, J.K Russell), *Rev Mineral* 24, 153 - 190;
- 677 Russell JK, Giordano D, Dingwell DB, Hess KU (2002) Modelling the non-Arrhenian rheology of  
678 silicate melts: Numerical considerations *Eur J Min* 14, 417–427
- 679 Russell JK, Giordano D, Dingwell DB (2003) High-temperature limits of non-Arrhenian silicate  
680 melts: Implications for modelling compositional dependencies *Am. Min.* 88, 1390-1394;
- 681 Russell JK, Giordano D (2005) A model for silicate melt viscosity in the System  $\text{CaMgSi}_2\text{O}_6$ -  
682  $\text{CaAl}_2\text{Si}_2\text{O}_8$ - $\text{NaAlSi}_3\text{O}_8$  *Geochim Cosmochim Acta* 69, 5333-5349;
- 683 Sahagian DI, Proussevich AA (1996) Thermal effects of magma outgassing *Jour Volcanol Geoth*  
684 *Res* 74, 19 - 38;
- 685 Stebbins JF, Carmichael, I.S.E, and Moret, L.K (1984) Heat capacities and entropies of silicate  
686 liquids and glasses *Contrib Mineral Petrol* 86, 131–148;
- 687 Toplis MJ (1998) Energy barriers to viscous flow and the prediction of glass transition temperatures  
688 of molten silicates *Am Min* 83, 480–490;

- 689 Toplis MJ, Dingwell DB, Hess KU, Lenci T (1997) Viscosity, fragility and configurational entropy  
of melts along the join  $\text{SiO}_2\text{-NaAlSiO}_4$  Am Min 82, 979–990;
- 690  
691 Toplis MJ, Gottsmann J, Knoche R, Dingwell DB (2001) Geochim Cosmochim Acta 65, 1985-199;
- 692 Webb SL (2008) Configurational heat capacity of  $\text{Na}_2\text{O-CaO-Al}_2\text{O}_3\text{-SiO}_2$  melts Chem Geol 256,  
693 92–101
- 694 Weill DF, Hon R, Navrotsky A (1980) The igneous system  $\text{CaMgSi}_2\text{O}_6\text{-CaAl}_2\text{Si}_2\text{O}_8\text{-NaAlSi}_3\text{O}_8$ :  
695 variations on a classic theme by Bowen In: Hargraves R.B (eds) Physics of Magmatic  
696 Processes Princeton University Press, Princeton, 49-92;
- 697 Whittington AG, Bouhifd MA, Richet P (2009) The viscosity of hydrous  $\text{NaAlSi}_3\text{O}_8$  and granitic  
698 melts: Configurational entropy models Am Min 94:1-16

### Captions to Figures

- 701 **Figure 1.** The heat capacity curve ( $C_p$ ) from DSC experiment on glass  $\text{An}_{42}$  showing how  $T_g^{\text{onset}}$ ,  
702  $T_g^{\text{peak}}$  and  $T_g^{\text{liquid}}$  are defined. The  $C_p$  curve in the figure was generated after cooling and  
703 heating from the glassy state through the glass transition at 10 K/min. A successful  
704 measurement is indicated by the glass returning to the same value of  $C_p$  after each cooling (not  
705 shown here). The dashed line is the Maier Kelley (MK) fit to the glass heat capacity.
- 706  
707 **Figure 2.** Variation of  $C_p^s$ , (triangles)  $C_p^l$  (circles) and  $C_p^c$  (squares) as a function of  $\text{H}_2\text{O}$  content in  
708 variably hydrated (a) Etna trachybasalt (Giordano and Dingwell, 2003; Giordano et al. 2005)  
709 and (b) melts in the An-Di system. Lines in both panels define  $c_p^i = c_p^{\text{dry}} + a^i \text{H}_2\text{O} + b^i \text{H}_2\text{O}^2$   
710 fitted to each of the Etna trachybasalt  $C_p$  datasets allowing direct comparison with glasses and  
711 melts in the An - Di system in (b).
- 712  
713 **Figure 3.** Values of  $C_p^s$  (triangles),  $C_p^l$  (circles) and  $C_p^c$  (squares) for all samples (Table 1) plotted as  
714 a function of (a)  $SM_{\text{hydrous}}$  and (b)  $NBO/T_{\text{hydrous}}$ . Symbols are as in Figure 2. Values of  $C_p^s$  and  
715  $C_p^l$  show a general decrease with increasing depolymerization, i.e., increasing  $SM_{\text{hydrous}}$  and  
716  $NBO/T_{\text{hydrous}}$ . In particular, the more polymerized compositions of the An-Di system ( $\text{An}_{100}$ ,  
717  $\text{An}_{90}$ ) have higher  $C_p^s$  and  $C_p^l$  than Etna trachybasalt that in turn have higher  $C_p^s$  and  $C_p^l$  and  
718 are more depolymerized than  $\text{An}_{42}$  and  $\text{An}_{90}$ . Absolute variations of  $C_p^c$  are also shown and can  
719 correspond to as much as 20 % relative (see text).
- 720  
721 **Figure 4.** Variation of  $C_p^s$  (triangles),  $C_p^l$  (circles) and  $C_p^c$  (squares) shown as a function of (a)  $\text{H}_2\text{O}$   
722 (mol%) and (b)  $SM_{\text{hydrous}}$  for samples measured here (Fig. 3) combined with the measurements  
723 of Bouhifd et al (2006). (a) Data plotted to show the effect of  $\text{H}_2\text{O}$  on the  $C_p$  of the more  
724 depolymerized melt tefritic compositions (Teph, NIQ; Bouhifd et al. 2013). The overall effect  
725 of  $\text{H}_2\text{O}$  on  $C_p$  of these depolymerized compositions is similar to that shown for the Etna  
726 trachybasalts. (b) Inclusion of the literature data allows  $C_p$  variations to be examined over a  
727 much wider range of  $SM_{\text{hydrous}}$  values than has previously been possible. Largely, more  
728 polymerized melts have lower  $C_p^l$  and  $C_p^c$ , and higher  $C_p^s$  than depolymerized natural melts.  
729  $C_p^c$  increases at low  $SM_{\text{hydrous}}$  values until becoming constant at  $>35$  mol%.  $C_p^l$  and  $C_p^s$  appear  
730 to show apparent minima at SM values of 45 (see text).

732 **Figure 5.** Measured and modelled glass transition temperatures for silicate melts for which hydrous  
733 heat capacity data exist, including data reported here and data compiled from the literature  
734 (Table 2). (a)  $T_g^{liquid}$  (K) against  $T_g^{onset}$  (K) for the fully relaxed melt defined using  $C_p$  curves  
735 (Fig. 1); compiled data are from Giordano et al (2005, 2008), Bouhifd et al (2006, 2013) (Table  
736 1). All data plot above the 1:1 model line and can be modelled by an offset temperature of 57.5  
737 K. (b)  $T_g$  (K) values taken as the temperature at which  $\eta = 10^{12}$  Pa s as predicted by temperature  
738 dependent viscosity curves (e.g., Eq. 1; see text and Appendix) plotted against  $T_g^{onset}$  (K).

739  
740 **Figure 6.** Calculated fitting parameters for the Adam-Gibbs temperature dependent equation (Eqs.  
741 1, 2) for melt viscosity to thermochemical and viscosity datasets for melt compositions listed  
742 in Table 2. (a) Best estimate values returned for adjustable parameters  $B_{AG}$  and  $S^c(T_g)$  for 41  
743 anhydrous (black symbols) and hydrous (grey symbols) melt compositions assuming a  
744 common but unknown high temperature limiting viscosity ( $A$ ). The global fit uses 23 melts to  
745 constrain the value of  $A$  to -3.51 (black symbols); 18 other melts having fewer viscosity  
746 measurements were fit for values of  $B$  and  $S^c(T_g)$  assuming this same optimal value of  $A$  (grey  
747 symbols). Symbol sizes of hydrous melts are proportional to water content. (b) Measured  
748 values of  $\log \eta$  plotted against predicted values calculated with the optimal value of  $A$  and  
749 values of  $B_{AG}$  and  $S^c(T_g)$  obtained for individual melt compositions. Dashed lines denote +/-  
750 0.25 log units. Symbols as in (a). (c) Derivative melt properties, including glass transition  
751 temperature ( $T_g^{12}$ ) and melt fragility ( $m$ ), calculated from the model (Table 2) for anhydrous  
752 (black) and hydrous (grey) melts (see text); symbol size is proportional to water contents.

753  
754 **Figure 7.** Covariation of the  $B_{AG}/S^c(T_g)$  ratio with melt composition as expressed by the variables  
755 (a)  $H_2O$  mol% and (b)  $SM_{hydrous}$ .

756  
757 **Figure A1.** The  $1\sigma$  solution space for the Adam-Gibbs equation fitted to each of the datasets Ab, Jd,  
758 and Ne (Table A1). The confidence envelopes on the solution are shown as 2-D slices through  
759 the corresponding 3-D confidence ellipsoid. The plane through the 3-D ellipsoid is chosen to  
760 contain the solution and be parallel to one of the parameters  $A$ ,  $B$  and  $S^c$  making it a constant in  
761 that space (see text). (A)  $A$ - $B$  plane; (B)  $A$ - $S^c$  plane; and (C)  $B$ - $S^c$  plane.

762  
763 **Figure A2.** The entire Ab-Jd-Ne dataset (N=36) is fit to the Adam-Gibbs equation assuming that all  
764 three melt compositions share a common (but unknown) value of  $A$  and individual values of  $B$   
765 and  $S^c$ . Main figure compares the  $1\sigma$  confidence ellipses (dotted lines) on the optimal values of  
766  $B$  and  $S^c$  (solid circles) for each melt composition at the model value of  $A$  ( $-3.80 \pm 2.2$ ). Inset  
767 shows the level of misfit in values of  $\log \eta$  predicted from the global optimization. Dashed  
768 lines denote  $\pm 0.25$  log units of viscosity.

769  
770 **Figure A3.** Comparison of model curves for temperature dependent viscosity and measured data for  
771 Ab, Jd, and Ne melts (Table A1). The viscosity,  $C_p^c$ , and  $T_g$  (K) datasets for each melt  
772 composition are fit simultaneously to model Adam-Gibbs curves (Eq. A3) assuming that there  
773 is a single common value of  $A$  ( $-3.8$ ). The shaded fields are the  $1\sigma$  confidence limits for the  
774 model functions derived from the confidence ellipses shown in Figure A2.

775  
776 **Figure A4.** Estimates of  $S^c(T_g)$  for three silicate melts (Ab, Jd, Ne) plotted against composition  
777 represented by  $SiO_2$  content (mol. %). The original results of Toplis et al. (1997) are  
778 reproduced here (cf. their Fig. 8b) and compared to the estimates obtained in this work where  
779 we assume the three melts share a common value of  $A$ .



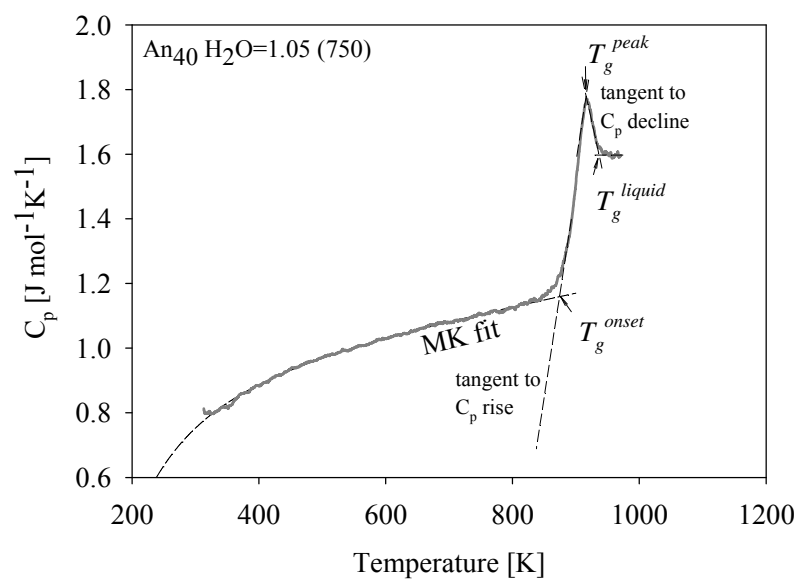
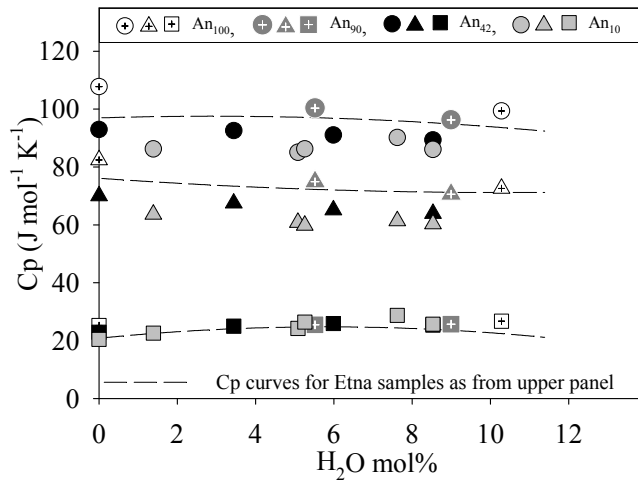
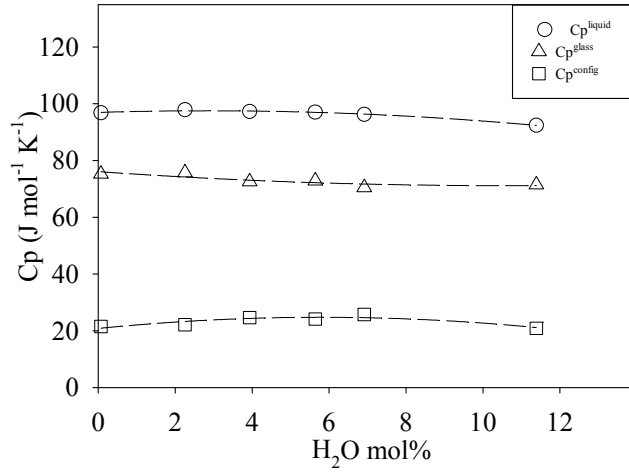


Figure 1. Giordano et al. (2015) [CMP]

Figure 2 Giordano et al. (2015) [CMP]



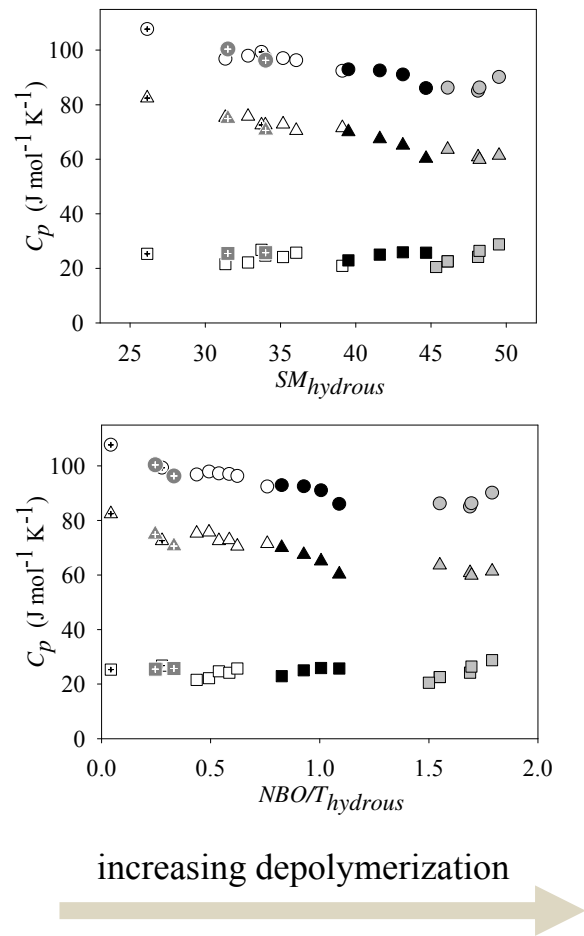
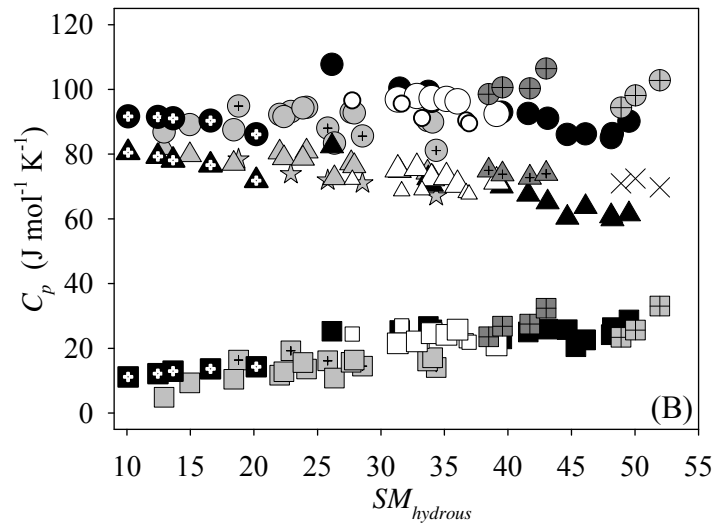
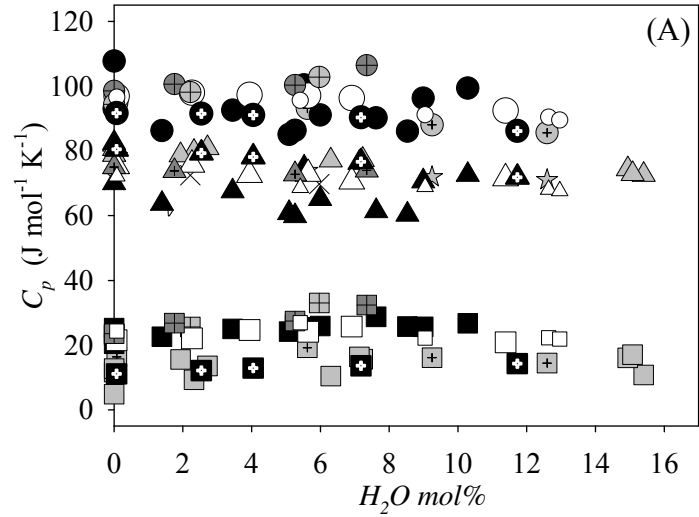


Figure 3. Giordano et al. (2015) [CMP]

Figure 4. Giordano et al. (2015) [CMP]



$C_p^l$	$C_p^g$	$C_p^c$	
⊕	⊕	⊕	PS pantellerite
●	△	■	samples from Bouhifd et al (2006)
○	△	□	Etna [this work,
○	△	□	Di Genova et al., 2014]
●	▲	■	all An - Di samples
⊕	▲	⊕	Teph
⊕	×	⊕	NIQ
⊕	☆	⊕	FR latite

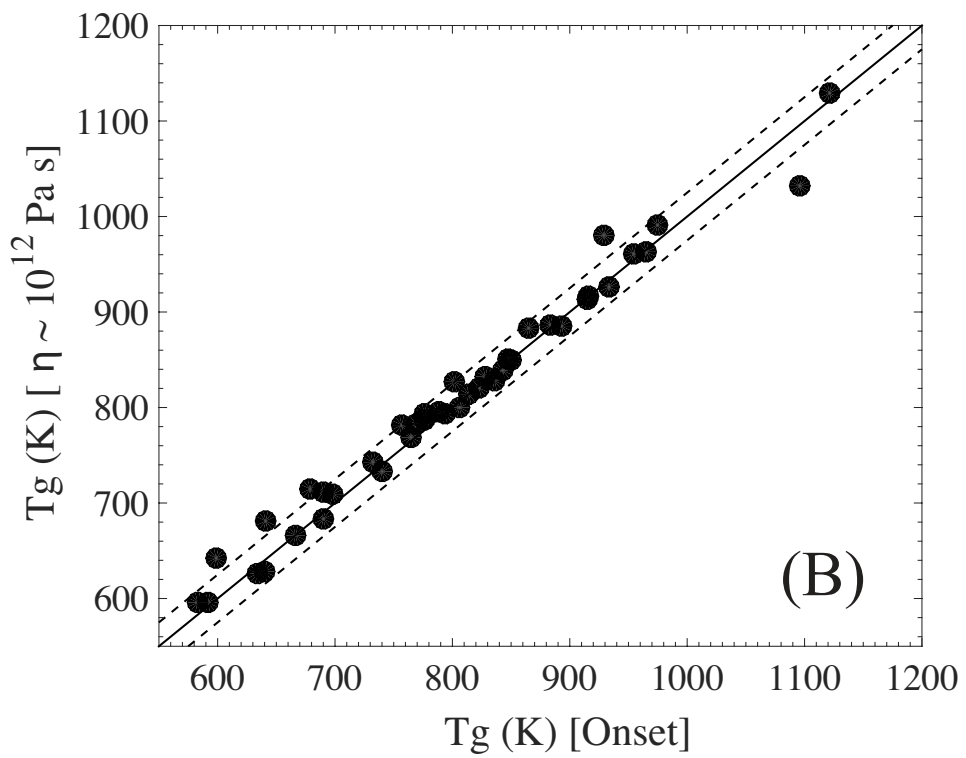
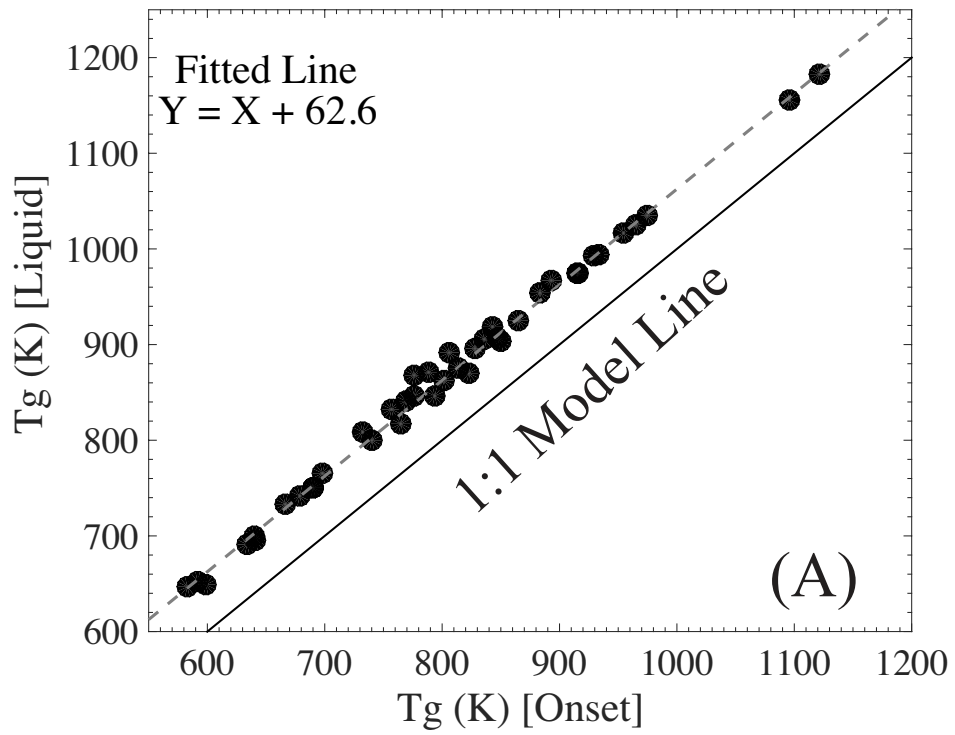


Figure 5. Giordano et al. (2014) [CMP]

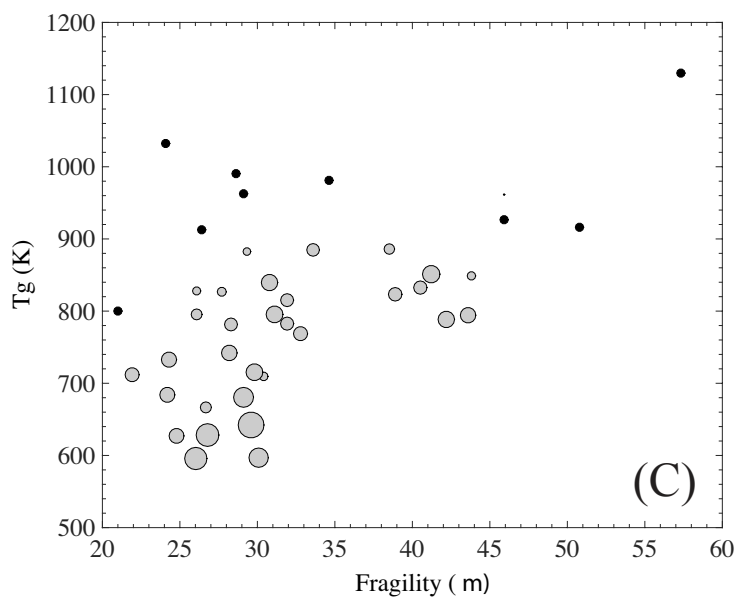
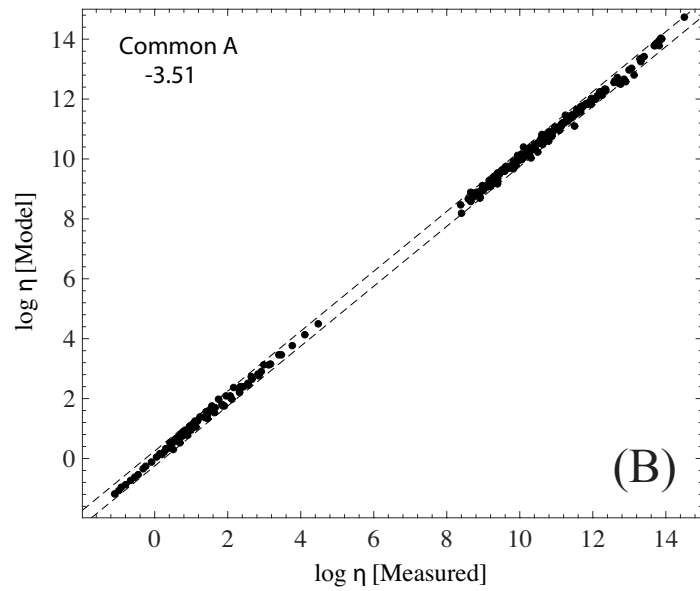
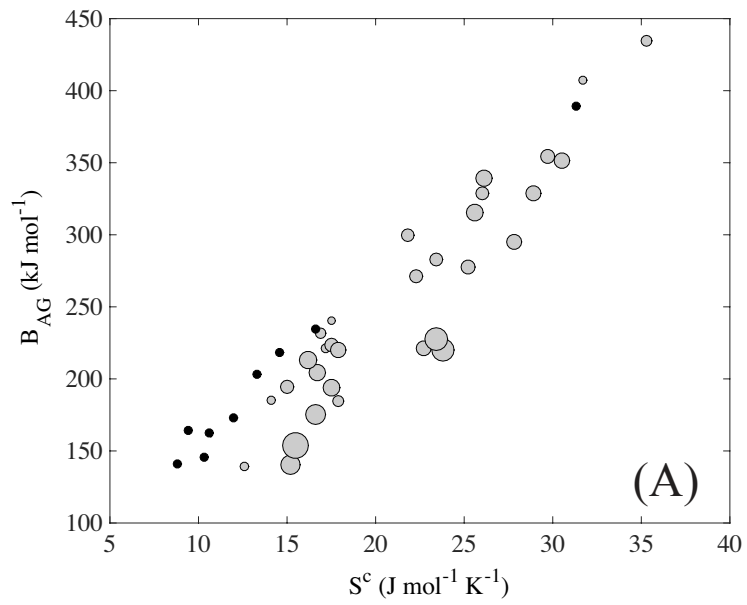


Figure 6. Giordano et al. (2014) [CMP]

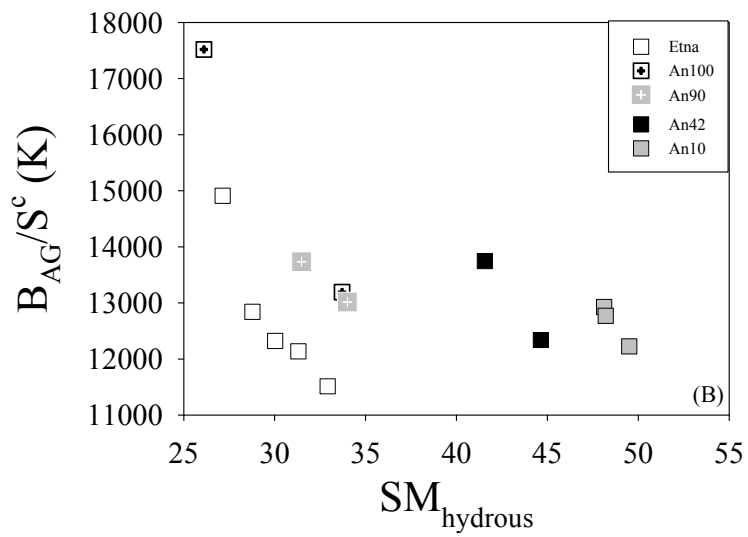
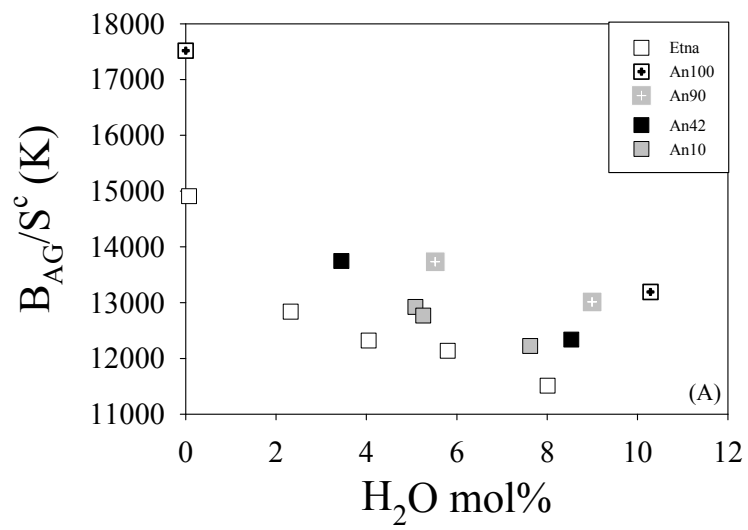


Figure 7. Giordano et al. (2015) [CMP]





**Table 2.** Summary of results derived from modelling of thermochemical and rheological experimental measurements. Data are divided into compositions used to constrain a common value of A (i.e. Global Fit) and compositions fitted using this optimal A-value (see text). N denotes the number of viscosity experiments. The model values reported include  $A_{AG}$  (-3.51),  $B_{AG}$ ,  $S^c$ , and the model calculated values of Tg (K) and fragility ( $m$ ).

Label	Source <sup>1</sup>	Experimental Measurements			AG (Global Fit: $A_{AG} = -3.51$ )			
		H <sub>2</sub> O wt. %	log $\eta$ N	$C_p^c$ J mol <sup>-1</sup> K <sup>-1</sup>	$B_{AG}$ J mol <sup>-1</sup>	$S^c$ J mol <sup>-1</sup> K <sup>-1</sup>	Tg K	Fragility $m$
<b>Used for Global Fit</b>								
ET	TW	0.02	10	21.05	160252	10.7	961	45.9
ET-801-1	TW	0.64	6	21.66	407278	31.7	828	26.1
BET1-3	TW	1.64	6	23.62	271133	22.3	783	31.9
An100	TW	0.00	66	25.29	164228	9.4	1130	57.3
An100H	TW	2.90	4	26.75	213279	16.2	851	41.2
An42Di58H3	TW	2.70	4	25.72	315456	25.6	796	31.1
HAB0	B	0.00	8	4.85	140779	8.8	1032	24.1
HAB2.2	B	1.87	8	10.45	277800	25.2	712	21.9
PHON0	B	0.00	20	11.68	234742	16.6	913	26.4
PHON0.5(B)	B	0.78	11	13.59	221059	17.2	827	27.7
PHON2.2	B	2.15	8	15.67	295090	27.8	684	24.2
TRACH	B	0.00	24	12.79	218516	14.6	963	29.1
TRACH50	B	0.57	9	15.59	240146	17.5	883	29.3
TRACH2.2	B	2.19	9	16.36	328571	28.9	733	24.3
TEPHDRY	B	0.00	22	23.54	172744	12.0	927	45.9
NIQ-0	B	0.00	20	23.36	145785	10.3	916	50.8
NIQ0.6	B	0.68	7	25.66	185250	14.1	849	43.8
DK89	B	0.00	14	8.93	162341	10.6	991	28.6
FR	D	0.0	12	18.08	202952	13.3	981	34.6
FR-1.6	D	1.59	4	24.74	283054	23.4	781	28.3
PS	D	0.0	12	11.16	389039	31.3	800	21.0
PS-0.5	D	0.72	4	12.18	139020	12.6	709	30.4
PS-1.1	D	1.16	4	12.92	184876	17.9	667	26.7
<b>Fitted to A= -3.51</b>								
ET-800-1	TW	1.13	4	24.15	434701	35.3	795	26.1
ET-802-1	TW	2.31	3	25.03	351593	30.5	742	28.2
An90Di10H1	TW	1.53	3	25.48	299677	21.8	885	33.6
An90Di10H2	TW	2.56	4	25.72	339279	26.1	839	30.8
An42Di58H1	TW	1.05	3	25.02	231958	16.9	886	38.5
AN10Di90H2	TW	1.69	3	24.23	194494	15.0	833	40.5
AN10Di90H3	TW	1.75	3	26.42	223778	17.5	823	38.9
An10Di90H4	TW	2.58	3	28.76	204623	16.7	788	42.2
PHON5	B	4.72	3	16.06	220095	23.8	596	26.0
TRACH5	B	4.92	3	17.07	227639	23.4	628	26.8
TEPH1.5	B	1.60	3	27.49	328597	26.0	815	31.9
TEPH2.22	B	2.27	3	32.42	220010	17.9	794	43.6
NIQ1.88	B	1.88	3	33.02	354117	29.7	769	32.8
FR-2.7	D	2.69	5	16.120	194064	17.5	715	29.8
FR-3.8	D	3.76	3	14.490	175261	16.6	681	29.1
FR-6.3	D	6.32	3	14.040	153889	15.5	642	29.6
PS-2.2	D	2.11	3	13.680	221170	22.7	627	24.8
PS-3.5	D	3.55	4	14.280	140296	15.2	597	30.1

<sup>1</sup>Sources include this work (TW) and literature: (B) Bouhifd et al. (2006, 2013); (D) Di Genova et al. (2014).

## Appendix A. Modelling Methodology

Our goal is to gain insight into the energetics of the melt to glass transition. Specifically we would like to investigate the configurational entropy associated with the glass transition. Richet and Bottinga (1984) estimate the magnitude of residual configurational entropy at the glass transition temperature ( $S_c(T_g)$ ) from the calorimetric cycle using enthalpy and heat capacity data available for crystalline material and for the glass and melt counterparts. Toplis et al. (1997) explored another route for estimating  $S_c(T_g)$  by combining calorimetric measurements on glasses and melts and measurements of viscosity on the same melts (e.g., Richet and Bottinga, 1995; Richet and Neuville, 1992). The Adam-Gibbs theory provides a robust connection between the transport or relaxation properties of melts (i.e. viscosity) and their thermochemical properties (Adam and Gibbs, 1965; Richet, 1984):

$$\text{Log } \eta = A + \frac{B}{T S^c(T)} \quad . \quad (A1)$$

Toplis et al. (1997) fit the Adam-Gibbs model to measured values of melt viscosity and estimated values of configurational heat capacity for 3 melt compositions (Table A1) using an expanded form of Eq. A1 where  $S_c(T_g)$  occurs as an adjustable parameter. This approach has been adopted and modified by a number of other workers (e.g., Toplis, 1998; Webb, 2008; Whittington et al., 2009; Avramov, 2013).

### ***The Data***

Here we follow this same approach and apply the method to hydrous melts and glasses. The main difference is that we assume that all silicate melts converge to a single, common, but unknown, value at high temperature. This strategy has a sound theoretical basis, strong empirical support, and creates substantially more reliable estimates of the other adjustable parameters (cf. Russell et al. 2002; 2003; Russell and Giordano, 2005)). The approach is therefore to:

- i) synthesize hydrous melts below their solubility limits at high pressure and temperature and quench them isobarically to produce homogeneous unvesiculated hydrous glasses;

- ii) use differential scanning calorimetry to measure: the heat capacity of the glass ( $C_{p_g}$ ) immediately below  $T_g$  (i.e. the onset of  $T_g$ ) and of the melt ( $C_{p_m}$ ) immediately above  $T_g$ ;
- iii) calculate the configurational heat capacity ( $C_{p_c}$ ) as  $C_{p_m} - C_{p_g}$ ;
- iv) measure the high and low temperature viscosity of the same melt.

These datasets are integrated and used to constrain the Adam-Gibbs equation (Eq. A1) for describing the T-dependent viscosity of melts. The configurational entropy at the temperature of interest (T) is replaced by:

$$S_c(T) = S_c(T_g) + \int_{T_g}^T \frac{C_{p_c}}{T} dT \quad (A2)$$

where  $C_{p_c}$  is the configurational heat capacity of the melt-glass transition. Assuming that  $C_{p_c}$  is independent of T, integration of A2 and substitution into A1 provides the expression:

$$\log \eta = A + \frac{B}{T [S_c(T_g) + C_{p_c} \ln(T/T_g)]} \quad A3$$

where  $A$ ,  $B$  and  $S_c(T_g)$  are adjustable unknown parameters to be solved for by fitting A3 to experimentally measurements of  $C_{p_c}$ ,  $T_g$  and  $\eta$ .

### ***Optimization Philosophy***

Below we demonstrate our approach to fitting the Adam-Gibbs equation to experimental measurements of  $T_g$ ,  $C_{p_c}$ , and pairs of  $\eta:T(K)$  to obtain estimates of  $A$ ,  $B$  and  $S_c(T_g)$  (Eq. A3). We illustrate our philosophy by remodelling the data from Toplis et al. (1997) for Albite (Ab), Jadeite (Jd), and Nepheline (Ne) melts ( $m=3$ ). Each dataset suggests a system of  $n$  non-linear equations for each melt composition of the form:

$$\log \eta_i = A + \frac{B}{T_i [S_c(T_g) + C_{p_c} \ln(T_i/T_g)]} \quad \text{for } i = 1:n \quad (A4)$$

where the three adjustable parameters  $A$ ,  $B$ ,  $S_c(T_g)$  are unique unknowns for each melt composition and  $n$  is the number of measured pairs of  $\eta:T(K)$ .

As stated above, we have adopted the work of Russell et al. (2002; 2003) and Russell and Giordano (2005) and assumed that silicate melts approach a common high-temperature limiting value (i.e.  $A$ ). This implies a single unknown value of  $A$  for all melts. Toplis et al. (1997) optimizations of the Ab, Ne and Jd melts also yielded a very narrow range of individual  $A$ -values (Table A1; -2.38 to -2.53) and on that basis Webb (2008) adopted a single averaged value of  $A$  (-2.61) from Toplis (1998) for her modelling.

Thus, we have elected to fit Adam-Gibbs equations (Eq. A3) to the calorimetric ( $Tg$ ,  $Cp_c$ ) and viscosity datasets for Ab, Jd, Ne melts simultaneously (Table A1). We solve a single system of equations (cf. A4) comprising the  $m=3$  datasets by minimizing the function:

$$\chi_{min}^2(\mathbf{x}) = \sum_{j=1}^m \sum_{i=1}^{n_j} \left[ \frac{\log \eta_i - A - B_j / \left( T_i \left[ S_{c_j} + Cp_{c_j} \ln \left( \frac{T_i}{Tg_j} \right) \right] \right)}{\sigma_i} \right]^2 \quad (A5)$$

where  $\mathbf{x}$  denotes the solution vector comprising a common value of  $A$ , and  $2m$  values of  $B$  and  $S_c(Tg)$ , each. There are a total of 36 ( $\sum_j n_j$ ) observations of viscosity for the  $m$  melt compositions (Table A1). The objective function is weighted to uncertainties ( $\sigma_i$ ) on viscosity arising from experimental measurement.

### ***Covariance Analysis***

The form of the Adam-Gibbs function is non-linear with respect to the unknown parameters and, therefore, A5 is solved by conventional iterative methods (e.g., Press *et al.*, 1986). One attribute of using the  $\chi^2$  merit function (A5) is that, rather than consider a single solution that coincides with the minimum residuals, we can map a solution region at a specific confidence level (e.g.,  $1\sigma$ ; Press *et al.*, 1986). This allows delineation of the full range of parameter values (e.g.,  $A$ ,  $B_j$ , and  $S_{c_j}$ ) that can be considered equally valid descriptors of the experimental data at the specified confidence level (e.g., Russell *et al.*, 2002). Furthermore, the confidence limits accurately portray the magnitude and nature of covariances between model parameters.

Russell *et al.* (2002; 2003) showed that the non-linear character of non-Arrhenian models ensures strong numerical correlations between, and even non-unique estimates of, model parameters. One result of the strong covariances between model parameters is that wide ranges

of values can be used to describe individual datasets. This is true even where the data are numerous, well-measured, and span a wide range of temperatures and viscosities. Stated another way, there is a substantial range of model values which, when combined in a non-arbitrary way, can accurately reproduce the experimental data.

We illustrate these concepts explicitly by displaying the covariances between parameters for each of the three datasets fitted independently with unique values of  $A$ ,  $B$  and  $S_c$  (Fig. A1; Table A1). The  $1\sigma$  confidence envelopes on the optimal 3 parameter solutions define 3-D ellipsoids; the 2-D ellipses plotted in Figure A1 approximate those confidence envelopes on two parameters where the third parameter is fixed at the optimal solution. These ellipses are planes through the 3-D ellipsoid that contain the solution and are parallel to the fixed parameter. For example, Figure A1 shows the range of values of  $A$  and  $B$  permitted (and the apparent correlation) fixed at the optimal value of  $S_c$  and the magnitude and nature of their covariance. As might be expected given the form of equation A3, the model-induced covariance is strongest between  $B$  and  $S_c$ . An additional consequence of the model is the negative covariance between  $A$  and  $B$  vs. a positive covariance between  $A$  and  $S_c$ .

The magnitudes of covariance between adjustable parameters also varies for the individual melt compositions. These variations reflect 3 main elements, in decreasing order of importance: i) the degree of non-Arrhenian behaviour (i.e. fragility), ii) the temperature-distribution of data, and iii) the quality of the data. Near-Arrhenian melts with low fragility numbers (*cf.* Table A1) allow for wide ranging, but strongly correlated, parameter estimates (*cf.* Ab vs. Ne; Fig. A1).

### ***Optimization to a Common A***

The optimal parameters derived from simultaneous solution of the 3 datasets (Ab, Jd, Ne) assuming a common value of  $A$  are summarized in Table A1 and Figure A2. The original viscosity data are reproduced to within experimental uncertainty (Fig. A2, inset). In Figure A2, the  $1\sigma$  confidence limits on  $B$  and  $S_c$  are shown for a fixed value of  $A$  (i.e. optimal solution  $A = -3.8$ ). The confidence envelopes are computed by mapping boundaries of constant  $\chi^{2*}$  around the optimal solution in the manner described fully by Press et al. (1986). The optimal solution is defined by the minimum  $\chi^2_{\min}$  from which a value of  $\Delta\chi^{2*}$  (i.e.  $\chi^{2*} - \chi^2_{\min}$ ) is set; the value of  $\Delta\chi^{2*}$  depends on the degrees of freedom and the confidence level of interest.

The matrix  $\alpha(2m+1, 2m+1)$  is then calculated for the  $\chi^2_{\min}$  fit from

$$\alpha_{k,l} = \sum_{i=1}^n \frac{1}{\sigma_i} \left[ \frac{\partial y_i}{\partial x_k} \frac{\partial y_i}{\partial x_l} \right] \quad (\text{A6})$$

where  $\alpha(k,l)$  are the individual entries on the matrix and  $y_i$  are the functions (A4) evaluated at the solution. The covariance matrix ( $C$ ) to the problem is the inverse of  $\alpha$ .

We have portrayed the confidence limits as 2-D ellipses resulting from the projection of the solution onto a single plane where the other parameter ( $A$ ) is fixed at the optimal solution (e.g., Fig. A2). These 2-D ellipses are computed from the matrix equation:

$$\Delta\chi^{2*} = r \cdot [C_p]^{-1} \cdot r' \quad (\text{A7})$$

where  $C_p$  is calculated from  $[\alpha_p]^{-1}$  and  $\alpha_p$  is the 2x2 submatrix of the original matrix  $\alpha$  containing rows and columns of the parameters of interest (e.g.,  $S_{c\ Ab}$  and  $B_{Ab}$ ). The unknowns to this matrix equation are the two components of the relative displacement vector  $r$  (i.e.  $r_x$ ,  $r_y$  or  $r_{Sc}$ ,  $r_B$ ). In its quadratic form, equation A7 becomes:

$$r_x^2 C_p(1,1) + 2 r_x r_y C_p(1,2) + r_y^2 C_p(2,2) = \Delta\chi^{2*} \quad (\text{A8})$$

The coordinates are calculated by fixing one unknown (e.g.,  $r_y$ ) and solving A8 for its roots. Given arbitrary values of  $r_y$ , the values of  $r_x$  are computed from:

$$r_x = \frac{-r_y C_p(1,2) \pm \sqrt{(r_y C_p(1,2))^2 - C_p(1,1) (r_y^2 C_p(2,2) - \Delta\chi^{2*})}}{C_p(1,1)} \quad (\text{A9})$$

Operationally we search for coordinate pairs across the minimum and maximum range of values for  $r_y$  established by the relationship:

$$r_y = \pm \sqrt{\frac{-C_p(1,1) \Delta\chi^{2*}}{C_p^2(1,2) - C_p(1,1) C_p(2,2)}} \quad (\text{A10})$$

### ***Forward Modelling***

To the uninitiated, the range of values of  $B$  and  $S_c$  (Fig. A2) consistent with the experimental dataset (Fig. A2, inset) may be larger than expected. To illustrate and emphasize the consistency of these confidence envelopes with the original viscosity measurements we have calculated families of Adam Gibbs functions (Eq. A3) using the combinations of  $B$  and  $S_c$  that define the ellipses in Figure A2. The limits to the families of Adam Gibbs functions are denoted in Figure A3 by two dashed lines delineating a shaded field and are compared directly to the original viscosity measurements and to the optimal fit (solid line). The dashed lines are essentially the  $1\sigma$  confidence limits on the model function.

In all three cases the family of curves derived from the confidence envelopes (Fig. A2) define narrow bands that are entirely consistent with the measurement uncertainties on the original datasets. The experimental data are permissive of a wide range of values of  $B$  and  $S_c$ , however, the strong correlations between parameters (Fig. A2) control how these values are combined. Thus, even though a wide range of parameter values are considered, they generate a narrow band of Adam Gibbs functions that are entirely consistent with the experimental data.

### ***Compositional Dependence***

We conclude this appendix with a comparison of our model values of  $A$ ,  $B$  and  $S_c$  to the original work of Toplis et al. (1997). Our single value of  $A$  (-3.80) describes the three datasets well but is  $\sim 1$  log unit lower than the values obtained by Toplis et al. (1997). Our fitting strategy is different in that we use a fixed value of  $Cp_c$  (Table A1) taken from his paper whilst they employed a temperature dependent equation. Despite the slight difference in values, Toplis et al. (1997) obtained virtually the same  $A$  value for each of their melts supporting our concept of optimizing for a common  $A$ .

Our values of  $S_c$  are plotted in Figure A4 and agree well with the values estimated by Toplis et al. (1997) and reproduce the overall compositional pattern (e.g., dependence on  $\text{SiO}_2$  content). More data would be required to assess whether our slightly higher value for Ne and lower value for Ab are better estimates or not. Our values of  $B$  are very close numerically to those of Toplis et al. (1997), however, the relative values for the Ab and Jd melts are switched.

In the case of derivative properties, including  $T_g$  and fragility ( $m$ ), our model returns similar values and similar patterns to those calculated by Toplis et al. (1997) (Table A1). Ne is

the most fragile melt (37.6 vs. 33.9) and Ab melt is the strongest (26 vs. 22.6). The values of  $m$  obtained by simply fitting each viscosity dataset to a standard temperature dependent equation for non-Arrhenian melts (i.e. the Vogel-Fulcher-Tamman equation; Fulcher, 1925) agree more closely with our values (Ab: 26 vs. 24.2; Jd 28.3 vs. 27.7; Ne: 37.6 vs. 40.2). Estimated of glass transition temperatures ( $T_g \sim T$  where  $\eta = 10^{12}$  pa s) are also in good agreement with values obtained from modelling the viscosity data by itself (Table A2).

---

---

---



Supplementary material online

[Click here to download Electronic supplementary material: SUPPORTING\\_ONLINE\\_MATERIAL.pdf](#)